


Biomimetic multifunctional nanoparticles for improved radiotherapy and immunotherapy in cancer treatment

Jiale Chen^{a,1}, Pan Ran^{b,c,1}, Yizhao Xu^c, Mouna Khouchani^d, Xin Li^a, Ling Jian^c, Takoui Abdelmajid^d, Nadia Aittahssaint^d, Qian Yang^e, Jingyi Li^{b,*}, Long Zhao^{b,c,*} 

^a School of Basic Medical Sciences, Chengdu Medical College, Chengdu, 610500, PR China

^b The Second Affiliated Hospital of Chengdu Medical College, China National Nuclear Corporation 416 Hospital, Chengdu Medical College, Chengdu, 610051, PR China

^c Development and Regeneration Key Laboratory of Sichuan Province, School of Bioscience and Technology, Chengdu Medical College, Chengdu, 610500, PR China

^d Mohammed VI University Hospital, Cadi Ayyad University, Marrakech, Morocco

^e Center of Scientific Research, Chengdu Medical College, Chengdu, 610500, PR China

ARTICLE INFO

Keywords:

Tumor microenvironment
Bacterial membrane vesicles
Immunotherapy
Radiosensitizers

ABSTRACT

Radiotherapy represents a conventional approach in clinical cancer treatment, but suffers from insufficient DNA damage and limited tumor selectivity. Herein, bismuth oxyiodide quantum dots loaded hollow manganese dioxide (MB) nanoparticles was fabricated and subsequently wrapped with bacterial membrane vesicles (MVs) to create MB@MV nanoparticles. This biomimetic radiosensitizer is designed to enhance the efficacy of radiotherapy through a combined approach of tumor immunotherapy and oxygen delivery strategy. Upon systemic administration, MB@MV enhance tumor accumulation through specifically targeting the inflammatory milieu mediated by MVs, thereby activating dendritic cell-mediated innate immunotherapy. Concurrently, MB@MV demonstrate superior X-ray absorption, leading to effective DNA damage in tumor cells due to the high atomic number of bismuth. Notably, manganese dioxide react with the overexpressed H₂O₂ in the tumor microenvironment to alleviate hypoxia and fixing X-ray induced DNA damage in tumor cells, culminating in a multi-strategy approach to enhance radiotherapy sensitization. The findings from both *in vitro* and *in vivo* experiments demonstrate a significantly enhanced inhibition of tumor growth by MB@MV compared to tumors treated solely with X-ray. Overall, our multifunctional radiosensitizer MB@MV shows considerable promise in the field of tumor radiotherapy.

1. Introduction

Colon cancer is becoming an alarmingly prevalent and life-threatening concern worldwide. Current treatment methods, including chemotherapy and surgical procedures, suffer from inevitable limitations of recurrence, metastasis, and considerable patient pain [1]. Radiation therapy (RT) has emerged as an effective and frequently used curative adjuvant treatment in clinical settings. Approximately 70 % of colon cancer patients receive RT either as a standalone treatment or in combination with chemotherapy or surgery [2]. RT employs high-energy X-ray or γ -ray to kill cancer cells by directly damaging cell DNA or generating reactive oxygen species (ROS) that induce cell apoptosis [3]. Despite significant advancements in the physical delivery of ionizing radiation doses, many methods remain largely empirical. The

simplistic notion that higher radiation doses correlate with increased therapeutic efficacy often results in suboptimal outcomes and elevates the risk of radiation injury to normal tissues [4]. Therefore, it is essential to develop a more efficient and minimally invasive RT sensitization strategy for the treatment of colon cancer.

To enhance the efficacy of tumor radiotherapy, various radiosensitizers containing high atomic number (high-Z) elements, such as bismuth (Bi), gold (Au), and tantalum (Ta), have been developed. These materials interact with low-energy photons to release photoelectrons and Auger electrons, thereby amplifying radiation damage to tumor tissues [5]. Among these, Bi-based nanoparticles (NPs), relatively inert in biological environments, are of particular interest due to their high mass-energy absorption coefficients for X-ray [6]. Mei et al. demonstrated that nanosheets doped with Bi elements could effectively inhibit

* Corresponding authors. The Second Affiliated Hospital of Chengdu Medical College, No.4, North Section 4, Second Ring Road, Chengdu 610051, PR China.

E-mail addresses: lijingyi@cmc.edu.cn (J. Li), longzhao@cmc.edu.cn (L. Zhao).

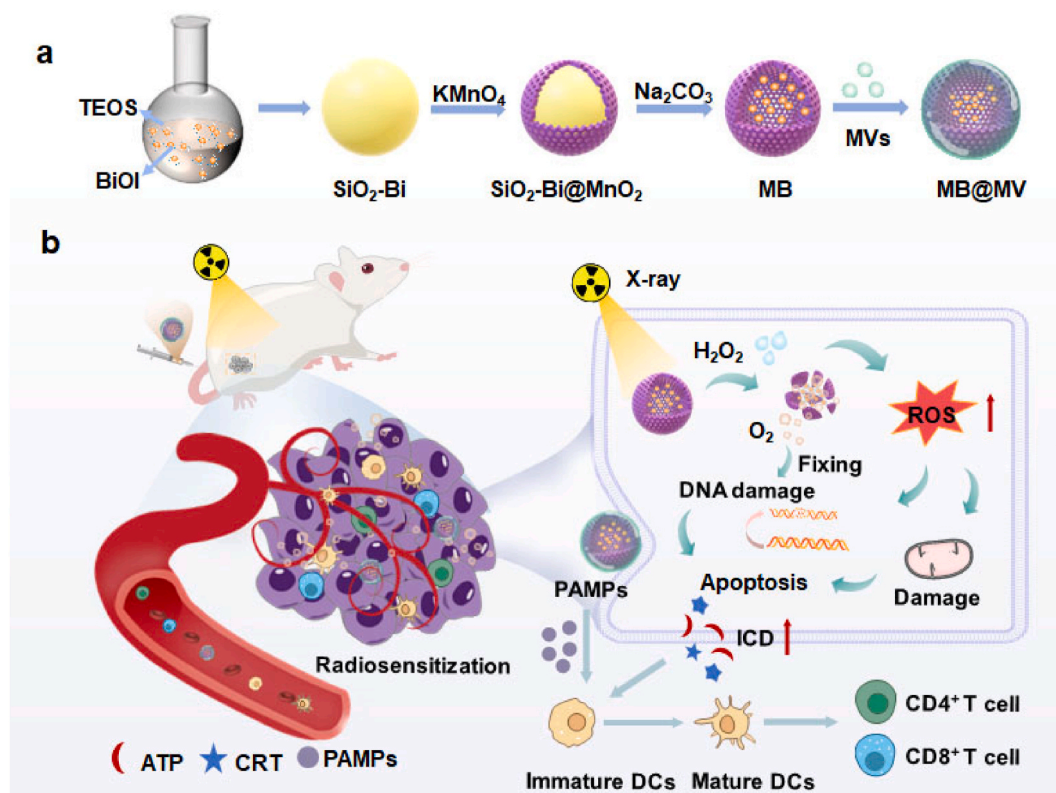
¹ The authors contributed equally to the work.

tumor growth and enhance the tumor-suppressive effect of radiotherapy under low-dose X-ray (4 Gy) irradiation [7]. However, high-Z radiosensitizers still face significant challenges for clinical translation. First, the hypoxic tumor microenvironment (TME) significantly compromises the efficacy of RT. Hypoxia not only reduces the generation of ROS, which are essential for radiation-induced DNA damage, but also promotes DNA repair mechanisms, leading to tumor resistance [8]. Second, the inability to precisely target tumor tissues often results in collateral damage to surrounding healthy tissues, causing severe side effects such as radiation-induced fibrosis, inflammation, and long-term organ dysfunction [9]. Therefore, in the field of radiotherapy sensitization, it is imperative to not only focus on the X-ray energy absorption effect but also address the pervasive issue of hypoxic TME.

In recent decades, various strategies have been explored to deliver O_2 into tumors to alleviate hypoxia. The most common approach involves using hemoglobin from red blood cells (RBC) or artificial O_2 carriers to deliver O_2 directly to the tumor. However, this delivery is limited by the structure and distribution of the tumor vasculature [10]. To address this issue, catalase or nanomaterials with catalase-like activity have been introduced into the tumor therapy. These agents continuously decompose endogenous hydrogen peroxide (H_2O_2), producing O_2 and alleviating the tumor's O_2 deficiency [11]. Among these, manganese dioxide (MnO_2) has a catalase-like activity, reacting with H^+ and H_2O_2 at the tumor site to produce O_2 , and exhibits better stability than catalase [12]. Chen et al. developed a nanocomplex CeO_2 - MnO_2 to function as a radiosensitizer. This nanocomplex enhances X-ray absorption at the tumor site due to the presence of the high-Z metal oxide CeO_2 . Additionally, it facilitates the release of O_2 through the reaction of MnO_2 with H_2O_2 within the tumor tissue, thereby mitigating hypoxia in the tumor region and contributing to improved efficacy of tumor radiotherapy

[13]. This demonstrated the significant potential of combining high-Z elements with in situ tumor O_2 production strategies. However, such research efforts are relatively rare, and the challenge of tumor targeting remains to be addressed.

Bacterial membrane vesicles (MVs) are biological membrane vesicles approximately 20–250 nm in size naturally produced by Gram-negative and Gram-positive bacteria [14]. Their unique properties, including biocompatibility, ease of modification, and ability to cross biological barriers, make them ideal candidates for targeted drug delivery [15]. Importantly, MVs are uniquely positioned as immunostimulatory agents for cancer therapy due to their distinct pathogen-associated molecular patterns (PAMPs). In contrast to Gram-negative bacterial outer membrane vesicles (OMVs) that primarily depend on lipopolysaccharide (LPS)-mediated immune activation - a mechanism associated with potential risks of systemic inflammatory responses [16], *Staphylococcus aureus*-derived MVs are completely devoid of LPS. Instead, they are enriched with diverse PAMPs, including pore-forming toxins and lipoteichoic acid, which provide alternative immunostimulatory pathways [17,18]. These components robustly engage Toll-like receptors to activate dendritic cells (DCs), drive cytokine production, and prime anti-tumor T-cell responses, mirroring the immunogenic effects of LPS without its toxicity [19]. Such distinctive immunological advantages, coupled with their inherent biocompatibility, make MVs a rational and innovative choice for the radiosensitization-immunotherapy platform. Previous studies have shown that MVs can activate various immune pathways to initiate anti-tumor immune responses. Rao et al. engineered Antares2-expressing MVs via gene knock-in, which activated caspase-1-mediated pyroptosis to elicit potent antitumor immunity and therapeutic efficacy [20]. Numerous studies have also highlighted the potential of MVs as a vaccine platform for cancer therapy [21].



Scheme 1. Preparation process and therapeutic mechanism of MB@MV NPs. (a) Synthesis route of MB@MV NPs. BiOI were loaded into SiO₂ layers and deposited with MnO₂ to create SiO₂-Bi@MnO₂ NPs, followed by selective etching of the SiO₂ layer to obtain MB NPs. MVs were wrapped onto the MnO₂ shell to acquire MB@MV NPs. (b) Systemic administration of MB@MV NPs enhanced tumor accumulation via MVs targeting. High-Z nature BiOI boosted X-ray absorption to enhance DNA damage effects, while MnO₂ reacted with H₂O₂ to produce O₂, which fixing DNA damage. Meanwhile, PAMPs induced DCs maturation and subsequent T cell infiltration, initiating a robust anti-tumor immune response.

However, to our knowledge, the combination of MVs-driven tumor immunity with an O₂-enhanced RT sensitization strategy has not yet been reported.

In current study, multi-functional NPs based on biomimetic modifications of MVs were developed for the synergistic treatment of immunotherapy and radiation sensitization. As shown in Scheme 1a, bismuth oxyiodide quantum dots (BiOI) were loaded into SiO₂ layers (SiO₂-Bi) and deposited with MnO₂ to create SiO₂-Bi@MnO₂ NPs, followed by selective etching of the SiO₂ layer to obtain MB NPs. MVs were wrapped onto the MnO₂ shell to acquire MB@MV NPs. After systemic administration, MB@MV NPs enhanced tumor accumulation through the targeted effects of MVs. Inside the tumor cells, MB@MV NPs can effectively improve X-ray absorption due to the high-Z nature of the BiOI that maximizes radiation dose deposition. Meanwhile, MnO₂ could react with the overexpressed H₂O₂ in the tumor, alleviating hypoxia and fixing the DNA damage at the tumor site to maximize the anti-tumor effect. In addition, PAMPs on the surface of MVs, as a potent adjuvant, induced DCs maturation and subsequent T cell infiltration, initiating a robust anti-tumor immune response, and RT-induced immunogenic cell death (ICD) promoted the translocation of reticular calreticulin (CRT) to the membranes of tumor cells, further enhancing this process (Scheme 1b).

The primary advantage of this antitumor nanosystem is the efficient synergy between immunotherapy and increased RT sensitivity through the incorporation of MVs and BiOI. This combination strategy significantly induced DNA damage and inhibited clonal formation. Besides, the hollow structure of MnO₂ facilitated the generation of O₂ for tumor hypoxia alleviation and improved the killing effect by fixing DNA damage and improving the loading efficiency of BiOI. In terms of biosafety, MB@MV NPs offered another advantage.

The MVs shell effectively prevented BiOI leakage during blood circulation, while the MnO₂ carrier was only degraded by TME. BiOI smaller than 10 nm could be cleared from the body by the kidneys, thus ensuring commendable cytocompatibility. Overall, we demonstrated the feasibility of this novel combination of MVs immunotherapy, hypoxia mitigation, and high-Z elements in improving tumor killing effect, which is promising for application in next-generation radiotherapy.

2. Materials and methods

2.1. Materials

Bi(NO₃)₃·5H₂O, Tween 20, potash iodide (KI), tetraethyl orthosilicate (TEOS), KMnO₄, ammonium hydroxide, L- α -phosphatidylcholine, cholesterol, and 1,2-dioleoyl-sn-glycero-3-phosphoethanolamine (DOPE) were obtained from Sigma-Aldrich Co. (St. Louis, MO, USA). Annexin V-FITC apoptosis detection kit, terephthalic acid (TA), Calcein 2',7-dichlorodihydrofluorescein diacetate (DCFH-DA), Cell Counting Kit-8 (CCK-8), calcein-AM/propidium iodide (PI), 4',6'-diamidino-2-phenylindole (DAPI), Camptothecin (CPT), 1,1'-Dioctadecyl-3,3',3'-Tetramethylindodicarbocyanine (Did) and adenosine triphosphate (ATP) content detection kits were obtained from Aladdin Reagent Co., Ltd (Shanghai, China). [Ru(dpp)₃]Cl₂ (RDPP) was obtained from Maokang biotechnology Co., Ltd (Shanghai, China). Penicillin-Streptomycin, Trypsin, fetal bovine serum (FBS), phenylmethylsulfonyl fluoride (PMSF), Dulbecco's modified Eagle's medium (DMEM), and Roswell Park Memorial Institute (RPMI) 1640 medium were purchased from Thermo Fisher Scientific Co., Ltd (Waltham, MA, USA). Bax, Bcl-2, and cleaved-caspase 3 antibodies were purchased from Cell Signaling Technology (CST, Boston, USA). Polyvinylidene fluoride (PVDF) membrane and ultrafiltration (MWCO 50 kDa) were purchased from Millipore Co. (MA, USA). Human umbilical vein endothelial cells (HUVECs), and mouse colon cancer (CT26) cells were obtained from the American Type Culture Collection (Rockville, MD, USA). All other chemicals were supplied by Changzheng Regents Co. (Chengdu, China), unless otherwise noted.

2.2. Preparation of MVs

Staphylococcus aureus was cultivated in Luria-Bertani broth at 37 °C for 12 h, allowing it to reach the logarithmic growth phase. After centrifugation at 5,000 rpm for 15 min, the culture supernatant was collected and filtered through a sterile 0.22 μ m pore size filter. Subsequently, the filtrate was ultracentrifuged at 160,000 rpm at 4 °C for 3 h [22]. The resulting pellet, containing the MVs, was vacuum-dried and rehydrated with 10 mL of PBS and stored at -80 °C.

2.3. Synthesis of MB@MV NPs

BiOI were loaded into SiO₂ layers and deposited with MnO₂ to create SiO₂-Bi@MnO₂ NPs, followed by selective etching of the SiO₂ layer. MVs were wrapped onto the MnO₂ shell to acquire MB@MV NPs (Scheme 1a). Briefly, KI (830 mg, 5 mmol) and Bi(NO₃)₃·5H₂O (429 mg, 1 mmol) were dissolved in 10 mL of water/ethanol mixture (1:3, v/v) and ultrasonicated for 30 min. After centrifugation at 12,000 rpm for 3 min, the supernatant was injected into 1 % Tween 20 aqueous solution. After another centrifugation at 8,000 rpm for 3 min, the supernatant was further treated with ultrafiltration to remove excess ions and Tween 20 [23]. The BiOI were collected and stored at -80 °C for further use.

To load BiOI into SiO₂ NPs, BiOI (1 mg) and TEOS (5 mL) were added to 165 mL of ammonium hydroxide (28 %)/water/anhydrous ethanol (1/4/28, v/v/v) under continuous stirring at 45 °C for 3 h. The precipitates were collected by centrifugation at 12,000 rpm for 10 min, and washed with anhydrous ethanol to obtain SiO₂-Bi NPs. [24]. Subsequently, 10 mL of KMnO₄ (30 mg/mL) solution was added dropwise to 10 mL of the SiO₂-Bi dispersion (4 mg/mL). After reacting at 37 °C for 6 h, the precipitates were collected by centrifugation at 10,000 rpm for 10 min and then washed with deionized water to acquire SiO₂-Bi@MnO₂ NPs, followed by redispersion in 20 mL of Na₂CO₃ (2 M) solution at 60 °C for 48 h to etch the SiO₂ layer [25]. The precipitate was collected by centrifugation at 12,000 rpm for 10 min and washed sequentially with distilled water and alcohol to obtain the MB NPs.

To coat MVs, MB NPs (1 mg/mL) were added to 5 mL of MVs suspensions and sonicated for 10 min, followed by extrusion through a 0.45 μ m polycarbonate membrane ten times. Subsequently, MB@MV NPs were collected by centrifugation and washed with PBS. Similarly, 5 mL of TEOS was added to 165 mL of ammonium hydroxide (28 %)/water/anhydrous ethanol (1/4/28, v/v/v) and stirred continuously at 45 °C for 3 h to acquire SiO₂ NPs. Then, 10 mL of KMnO₄ (30 mg/mL) was added to 10 mL of SiO₂ (4 mg/mL) dispersions and reacted for 6 h to collect SiO₂@MnO₂ precipitate. This solution was then dispersed in a 2 M of Na₂CO₃ aqueous solution and treated at 60 °C for 48 h to etch the SiO₂ layer. The resulting MnO₂ NPs were obtained by centrifugation. Finally, after coating with MVs, M@MV NPs were obtained.

To fluorescently label NPs, Did was inoculated into NPs suspensions at 1 μ g/mL to prepare MB@MV/Did NPs [26]. To prepare liposome-coated NPs, L- α -phosphatidylcholine (5 mg/mL), cholesterol (1.5 mg/mL), and DOPE (1.5 mg/mL) were dissolved in 2 mL of anhydrous chloroform. The mixture was then evaporated at 45 °C to form a lipid membrane, which was hydrated by adding 4 mL PBS and dispersed using a probe-type ultrasonicator for 30 min [27]. The collected liposomes were combined with MB, and the mixture was extruded through a polycarbonate membrane. Subsequently, the liposomes were labeled with Did to prepare MB@lip/Did NPs.

2.4. Characterization of MB@MV NPs

The size and thickness profiles of BiOI were analyzed by atomic force microscopy (AFM, Bruker Dimension ICON, Germany). The surface morphologies of SiO₂-Bi@MnO₂ and MB NPs were characterized by scanning electron microscopy (SEM, FEI Quanta 200, The Netherlands). The structural characteristics of BiOI, MVs, MB, and MB@MV NPs were observed by transmission electron microscopy (TEM, JEM-2100F, JEOL,

Tokyo, Japan) with equipped energy-dispersive X-ray spectroscopy for elemental composition analysis. The hydrodynamic diameter and zeta potential of SiO₂-Bi, SiO₂-Bi@MnO₂, MB, and MB@MV NPs were analyzed by dynamic light scattering (DLS, Malvern NanoZS90, UK). The elemental composition of MB@MV NPs was analyzed by X-ray photoelectron spectroscopy (XPS, Thermo Scientific K-Alpha, USA). The specific surface area and pore structure of SiO₂-Bi@MnO₂ and MB NPs were analyzed by Brunauer-Emmett-Teller (BET, Micromeritics, USA). To ascertain the MVs content, MB@MV NPs were extracted using RIPA lysis buffer (Beyotime, Shanghai, China) supplemented with PMSF protease inhibitor (1 mM). The total protein content in the lysate was determined with a bicinchoninic acid (BCA) kit by measuring the absorbance value at 562 nm. The lysate was boiled for 10 min and loaded for sodium dodecyl sulfate-polyacrylamide gel electrophoresis (SDS-PAGE) analysis (Bio-Rad PowerPac, USA).

2.5. *In vitro* O₂ generation and MnO₂ degradation

The O₂ generation of MB@MV NPs was determined after incubation with H₂O₂ (1 mM), using PBS, FBS, and H₂O₂ (1 μ M) as controls. Briefly, MB@MV NPs suspensions (200 μ g/mL) were incubated with H₂O₂ (1 mM) at 37 °C for 15 min. At each specified interval, the O₂ levels were measured using a dissolved O₂ analyzer (Kolida Instrument, Guangzhou, China). In addition, the O₂ levels of MB@MV NPs treated CT26 cells detected by using RDPP fluorescent probes as capture agents. Briefly, CT26 cells were cultured in DMEM supplemented with 10 % FBS and seeded on 24-well tissue culture plates (TCPs) at 2×10^4 cells per well for 24 h. Thereafter, deferoxamine (200 μ g/mL) was added to construct a hypoxic environment. After incubation with MB@MV NPs (200 μ g/mL) for 12 h, the RDPP (10 mg/L) was added and incubated for 15 min, fixed with 4 % paraformaldehyde, and stained with DAPI (1 μ g/mL). Fluorescence images of cells were captured with confocal laser scanning microscopy (CLSM, Nikon A1, Japan). To evaluate the degradation capacity of MnO₂ NPs *in vitro*, we simulated normal tissue (pH 7.4, 1 μ M H₂O₂), TME (pH 6.5, 100 μ M H₂O₂), and intracellular tumor (pH 5.5, 1 mM H₂O₂) environments [28,29]. MB NPs at a 200 μ g/mL concentration were then dispersed in the various PBS solutions described above. The samples were incubated at 37 °C and collected after 1 and 2 h. The morphologies were then observed by TEM.

2.6. *In vitro* hydroxyl radical (•OH) generation

The yield of •OH from M@MV and MB@MV NPs was determined by monitoring the change in fluorescence intensity of the fluorescent probe TA [30]. Briefly, M@MV and MB@MV NPs (1 mg) were mixed with 5.0 mL of a TA (5 mM) solution containing 1 mM H₂O₂ at pH 5.5 and incubated at 37 °C for 30 min. Samples were irradiated with different doses (1, 2, 4, and 6 Gy) using an X-ray irradiator (PXI X-RAD 225, China) and finally detected by fluorescence spectrophotometry (Hitachi F-2700, Japan) at excitation/emission wavelengths of 315/420 nm.

2.7. *In vitro* cellular uptake of MB@MV NPs

The internalization efficiency of CT26 cells was examined after incubation with Did-labeled MB@MV/Did NPs, using MB@lip/Did as controls. Briefly, CT26 cells were seeded in 24-well TCPs at 2×10^4 cells per well and treated with different concentrations of NPs for 24 h. At specific time points, cells were harvested and lysed with RIPA lysis buffer at 4 °C for 30 min. The fluorescence intensity of Did in the lysates was measured via fluorescence spectrophotometry to determine uptake efficiency. In another batch of assays, cells were fixed with 4 % paraformaldehyde for 30 min, counterstained with 1 μ g/mL DAPI, and observed under CLSM to visualize NPs internalization [31].

2.8. Intracellular ROS generation and anti-tumor efficiency

The generation of intracellular ROS in CT26 cells was detected using DCFH-DA fluorescent probes after different treatments (PBS, MB@MV, RT, M@MV/RT, MB/RT and MB@MV/RT). Briefly, CT26 cells at 2×10^4 cells per well were cultured for 24 h and then incubated with NPs (200 μ g/mL) for 6 h. After 6 Gy of X-ray irradiation, the cells were treated with DCFH-DA (10 μ g/mL) for 30 min and then observed using CLSM [32].

CT26 cells were seeded in 96-well TCPs at 5,000 cells per well and co-cultured with MB@MV NPs (200 μ g/mL) for 6 h, and then exposed to various irradiation doses (0, 0.5, 1, 2, 4, 6, and 8 Gy). Afterwards, CCK-8 was added and incubated for 1 h, and the cell viability was evaluated through a microplate reader (Thermo Fish Scientific, USA) by detecting absorbance at 450 nm. Besides, the CT26 cells killing efficiency was examined in terms of calcein-AM/PI staining, cell viability, cloning, and apoptosis evaluation after treatment with MB@MV/RT, using MB@MV, RT, M@MV/RT, MB/RT, and PBS as controls. Briefly, CT26 cells were seeded in 96-well TCPs at 5,000 cells per well and co-cultured with NPs (200 μ g/mL) for 6 h, and then exposed to irradiation doses 6 Gy. Afterwards, CCK-8 was added and incubated for 1 h, and the cell viability was evaluated through a microplate reader by detecting absorbance at 450 nm. In another batch of experiments, cells were stained with calcein-AM/PI according to the manufacturer's protocol, followed by an inverted fluorescent microscope (Olympus IX71, Japan) observation [33]. To visualize CT26 cells, MB@MV/RT-treated cells were cultured at 37 °C, and the media changed every two days until visible cell colonies formed. The cells were then fixed with 4 % paraformaldehyde and stained with crystal violet for visual observation [34]. The apoptosis of CT26 cells was quantified by an Annexin V-FITC apoptosis detection kit according to the manufacturer's instructions [35]. Briefly, CT26 cells were seeded into 6-well TCPs at a density of 1×10^5 cells per well and treated with MB@MV/RT as described above. The floating and attached cells were washed with PBS and suspended in 500 μ L of binding buffer. After the addition of 5 μ L of Annexin V-FITC and 5 μ L of PI, the sample was incubated at 37 °C for 20 min, washed with PBS, and analyzed with flow cytometry (NovoCyte Advanteon, Agilent, USA).

2.9. Anti-tumor mechanism of MB@MV NPs CT26

The anti-tumor mechanism of MB@MV/RT was investigated on CT26 cells, using PBS, MB@MV, RT, M@MV/RT, MB/RT and positive CPT as controls. CT26 cells at 2×10^4 cells per well were cultured for 24 h and then incubated with NPs (200 μ g/mL) for 6 h, after 6 Gy of X-ray irradiation, and then incubation for another 24 h. Besides, the positive control was treated with CPT (5 μ M) for 12 h. Treated were permeabilized with 0.1 % Triton X-100 and blocked with 2 % BSA buffer for 1 h. The anti-phospho-histone H₂AX (γ -H₂AX) mouse monoclonal antibody (1:200) was incubated with CT26 cells at 4 °C for 24 h, and then incubated with goat anti-mouse secondary antibody (CoraLite 594, 1:1000) at 37 °C for 2 h. Cells were counterstained with DAPI (1 μ g/mL), and fluorescence images were captured by CLSM [36]. In another batch of assays, the positive control carbonyl cyanide m-chlorophenyl hydrazone (CCCP, 10 μ M) provided in the JC-1 kit (Solarbio, China) was added to the CT26 cell culture medium, and the CT26 cells were treated for 20 min. CT26 cells were stained using the JC-1 kit according to the manufacturer's instructions and subsequently observed with CLSM.

Western blotting was employed to investigate changes in protein expression following various treatments. The treated cells were incubated with RIPA lysis buffer supplemented with PMSF (1 mM) protease inhibitor at 4 °C for 30 min. The extracted proteins were then boiled for 10 min and loaded for PAGE analysis. Following this, the proteins were transferred to a PVDF membrane and blocked with a solution of 5 % skim milk powder. The PVDF membrane was incubated with primary and secondary antibodies for Bax, Bcl-2, and cleaved-caspase 3. The protein expression levels were detected using a gel imager (Bio-Rad

PowerPac, USA).

2.10. *In vivo* tumor target and treatment efficacy

A colon cancer model was established to investigate the target effect of MB@MV NPs, using MB@lip NPs as controls. All animal experimental protocols were approved by the Animal Care and Use Committee of Chengdu Medical College and were conducted in strict accordance with the Institutional Health Guide for the Care and Use of Laboratory Animals of China. Briefly, female Balb/c mice (8 weeks old) were obtained from Sichuan Dashuo Biotech (Chengdu, China) and subcutaneously injected with 100 μ L of CT26 cells suspensions (1×10^6 cells). Tumor growth was monitored until the tumor volume reached 100 mm³ to establish the colon cancer model. MB@MV/Did and MB@lip/Did NPs were injected into the tail vein of colon cancer-bearing mice, respectively. At predetermined time points, fluorescence images were captured using the Xenogen IVIS Spectrum Imaging System (Caliper Life Sciences Inc., USA) with the excitation/emission wavelengths of Did at 646/663 nm. After administration for 8 h, mice were euthanized, and the major tissues (liver, heart, spleen, lungs, and kidneys) were harvested for imaging.

To assess the *in vivo* hypoxia-relieving effect of MB@MV NPs, tumor-bearing mice were treated with MB@MV NPs (200 mg/kg), MVs, MB, or PBS as controls. Eight h post-administration, O₂ levels were evaluated using photoacoustic (PA) computerized tomography (Endra Nexus 128, USA) [37]. To evaluate the *in vivo* antitumor effect of MB@MV NPs, colon cancer-bearing mice were randomly divided into six groups (PBS, MB@MV, RT, M@MV/RT, MB/RT, and MB@MV/RT, $n = 6$). Mice in each group were injected with 100 μ L of NPs at a concentration of 200 mg/kg through the tail vein, with or without 6 Gy of X-ray irradiation administered 8 h after the injection. The tumor volume of the mice was measured every 3 days, with tumor volume calculated using the formula: Tumor volume = (length \times width²)/2. Survival curves were plotted using the Kaplan-Meier method, and median survival time was calculated to compare treatment efficacy. After 24 days of treatment, mice were sacrificed, and tumors were harvested and fixed in 4 % neutral buffered formalin. Hematoxylin and eosin (H&E) staining was performed to assess histological changes. To examine DNA damage, immunofluorescence staining images of γ -H₂AX was conducted on tumor sections. To investigate tumor cell proliferation and apoptosis, immunohistochemical (IHC) staining for Ki-67, TUNEL, and caspase-3 was performed on tumor sections, as described previously [38].

2.11. Immune activation effect of MB@MV NPs

To analyze the expression of CRT on the cell surface, CT26 cells were inoculated into 24-well TCPs and subjected to various treatments (PBS, MB@MV, MB/RT, MB@MV/RT) for 6 h, irradiation at a dose of 6 Gy. After being cleaned and fixed by standard immunofluorescence methods, CT26 cells were treated with anti-CRT primary antibody and goat anti-rabbit IgG (CoraLite 647, Proteintech Group, China) labeled secondary antibody, and stained with DAPI for CLSM observation [39]. ATP content was detected by ATP detection kit. CT26 cells were collected and incubation with ATP extract kit, and the absorbance was measured at 340 nm after ultrasonic lysis [40].

To detect DCs maturity *in vitro*, 8-week-old female Balb/c mice were selected. After euthanasia, the muscle tissue around the mouse femur was excised. The femoral bone cavity was subsequently rinsed with sterile PBS to obtain a cell suspension. The cells were filtered through a 70 μ m cell filter (300 g, 5 min) and then added to RBC lysis buffer (Solarbio, China) for 3 min and collected (400 g, 5 min). The cells were washed twice with PBS containing 2–3 % Penicillin-Streptomycin and centrifuged (300 g, 5 min). Finally, the cells were resuspended in RPMI 1640 complete medium containing 10 ng/mL granulocyte-macrophage colony-stimulating factor (GM-CSF, Novoprotein, China) for 6 days to obtain immature bone marrow-derived dendritic cells (BMDCs). Then,

BMDCs were incubated in 24-well TCPs at a density of 2×10^4 cells per well. Various treatments were applied, including PBS, MB@MV, MB/RT, and MB@MV/RT. After treatment, the cells were collected, stained with anti-CD80-APC and anti-CD86-PE (BioLegend, USA) antibodies, and analyzed using flow cytometry to evaluate the expression of these surface markers [41].

To investigate immune cells in lymph nodes and tumors, we collected tumor-draining lymph nodes and tumors after administering various treatments to tumor-bearing mice (PBS, MB@MV, MB/RT, and MB@MV/RT). A single-cell suspension was prepared using 1 mg/mL collagenase IV (Sigma-Aldrich, USA), 100 mg/mL DNase I (Sigma-Aldrich, USA), and 0.01 % trypsin at 37 °C in a 5 % CO₂ to digest tumor tissues and lymph nodes. The resulting single-cell suspension was filtered through a 70 μ m cell filter and washed with RPMI-1640 medium supplemented with 2 % FBS. Subsequently, the single-cell suspensions were stained with a variety of antibodies. Anti-CD80-APC and anti-CD86-PE were used to stain DCs in the lymph nodes. Additionally, anti-CD3-FITC (BioLegend, USA), anti-CD4-APC (BioLegend, USA), and anti-CD8a-PERCP (BioLegend, USA) antibodies were utilized to stain T cells within the tumor. Finally, the tumor tissues were fixed, and IHC staining for CD4⁺ and CD8⁺ was performed on the tumor sections. The sections were subsequently examined under a microscope.

2.12. Safety evaluation of MB@MV NPs

Cytotoxicity and hemolysis assays were performed to evaluate the *in vitro* safety of NPs. Briefly, HUVECs were initially seeded onto a TCPs for 24 h. Cells were incubated with a DMEM containing various concentrations of MB@MV NPs (0, 10, 50, 100, 200, and 400 μ g/mL) for 24 h. Cell cytotoxicity was assessed using the CCK-8 assay after 1 h incubation. For the live/dead staining assay, cells from each group were treated with calcein-AM/PI staining for 15 min, and images were captured using an inverted fluorescent microscope [42].

The hemolytic activity of MB@MV NPs was assessed after incubation with RBC. Briefly, RBC were isolated from mouse blood via centrifugation. A 50 μ L aliquot of fresh RBC suspension was then incubated with varying concentrations of MB@MV NPs for 4 h. The release of hemoglobin from RBC was measured by determining the absorbance at 540 nm. The hemolysis rate was calculated by comparing the hemoglobin levels released in pure water (positive control) and PBS (negative control) [43].

The body weights of mice after different treatments were measured every 3 days. At the end of the indicated treatment, major organs, including the heart, liver, spleen, lungs, and kidneys, were harvested for histopathological examination through H&E staining [44]. To evaluate safety *in vivo*, normal mice were injected via the tail vein with 100 μ L of either PBS or MB@MV NPs (200 and 400 mg/kg). The mice were sampled after 14 d. Blood was collected under anesthesia, and hematological and biochemical analyses were performed.

2.13. Statistical analysis

Experimental data were expressed as mean \pm standard deviation. Analysis of variance (ANOVA) was employed to compare multiple groups, and a two-tailed Student's t-test was used to determine statistical differences between the two groups. A probability value (p) less than 0.05 was considered statistically significant.

3. Results and discussion

3.1. Characterization of MB@MV NPs

Radiotherapy as a widely adopted tumor treatment strategy has attained a moderate success in clinical applications. Nevertheless, it suffers from inadequate DNA damage and restricted tumor selectivity. Moreover, tumor recurrence poses a formidable conundrum for the

current therapeutic regimens. In light of these circumstances, we have conceptually designed multifunctional MB@MV NPs for the precise treatment of colon cancer. These NPs are loaded with BiOI that enhance X-ray absorption and release O_2 , thereby enhancing DNA damage and preventing its repair. Meanwhile, MVs are used to stimulate the immune system and amplify the killing effect of radiotherapy, thereby achieving the selective eradication of tumor cells. Fig. 1a showed AFM images of BiOI, demonstrating uniform particle size and a fine dispersion effect. 100 quantum dots were randomly selected from different AFM images for statistical analysis of the particle size distribution, showing a uniform size with an average diameter of 6 nm. Moreover, thickness profiles of BiOI shows similar diameter along line 1 (5.68, 6.09 nm) and line 2 (5.99, 6.34 nm) (Fig. 1b). TEM results showed that the size of BiOI belonged to the quantum dots region (<10 nm) (Fig. 1c), which could be filtered and excreted from living animals through the kidneys to improve its biosafety [23]. The BiOI were encapsulated into SiO_2 via consolidated Stober method [45], and coated with MnO_2 as a shell, followed by etching the SiO_2 layer to construct MB NPs. Fig. S1a showed SEM observations of SiO_2 -Bi@ MnO_2 NPs, indicating spherical nanostructures with uniform sizes of about 135 nm, while MB NPs exhibited a hollow morphology and a rough surface with similar size (Fig. 1d). TEM results showed that the MB NPs exhibited a spherical hollow structure, and BiOI were dispersed in the interior of MB NPs (Fig. 1e). Fig. S1b presents the nitrogen adsorption-desorption isotherms and pore size distributions for SiO_2 -Bi@ MnO_2 NPs and MB NPs. The MB NPs demonstrated a type-IV isotherm with H1 hysteresis loops of mesoporous materials [46]. The calculated BET-specific surface area for MB NPs was $140.3\text{ m}^2/\text{g}$, which was significantly larger than that of non-porous SiO_2 -Bi@ MnO_2 NPs ($33.1\text{ m}^2/\text{g}$). The Barrett-Joyner-Halenda (BJH) analysis revealed a pore distribution ranging with a prominent peak at 12 nm, highlighting the mesoporous

structure of MB NPs.

MVs are non-replicating nano-spherical bilayer vesicles secreted by bacteria, with a diameter ranging from 20 to 300 nm [47]. TEM images of MVs revealed a uniform nanovesicle structure with an average size of 50 nm (Fig. 1f), and MB@MV NPs displayed a distinct core-sheath structure and an average size of 150 nm (Fig. 1g). Elemental mapping depicted that P and Bi elements were positioned around the manganese core. SDS-PAGE analysis indicated that the components of membrane proteins were mostly retained throughout NPs fabrication (Fig. 1h), indicating the successful wrapping of MVs around MB NPs. The hydrodynamic sizes of SiO_2 -Bi, SiO_2 -Bi@ MnO_2 , MB, and MB@MV NPs were around 108, 149, 155, and 177 nm (Fig. S2a). These sizes are larger than those observed in SEM and TEM, likely due to the hydration layer that forms on the surface of the NPs, which affects particle size measurements. The zeta potential of SiO_2 -Bi@ MnO_2 NPs changed from -15.7 mV (SiO_2 -Bi) to -11.3 mV , attributed to the positive charge of MnO_2 [25], and there was a slight variation to -12.8 mV (MB) after etching the SiO_2 layer, and decreased to -15.6 mV after MVs encapsulation (Fig. S2b).

As shown in Fig. 1i, the XPS survey spectra of MB@MV NPs showed detectable signals of P 2p from MVs, and Bi 4f and Mn 2p from MB NPs. The high-resolution spectra of Bi 4f showed two characteristic peaks at 164.6 eV (Bi $4f_{5/2}$) and 159.2 eV (Bi $4f_{7/2}$) from BiOI (Fig. 1j), and the characteristic peaks of 654 eV (Mn $2p_{1/2}$) and 642.5 eV (Mn $2p_{3/2}$) from MnO_2 (Fig. 1k), indicating the successful preparation of MB NPs. The characteristic peak at 133.1 eV in the P 2p spectrum was ascribed to MVs components from MB@MV NPs (Fig. 1l). The XPS patterns implied the successful loading of BiOI and the existence of MVs components from MB@MV NPs.

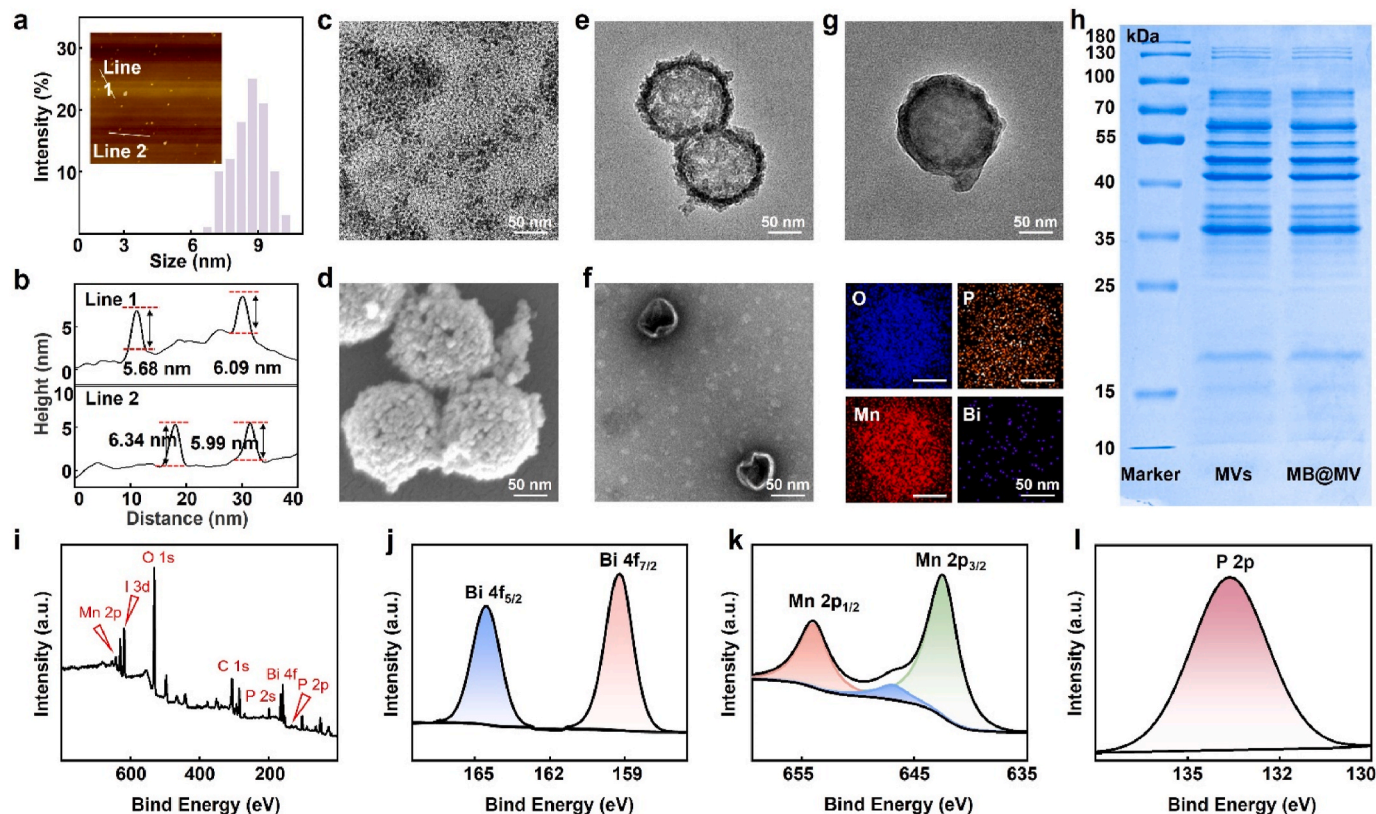


Fig. 1. Characterization of MB@MV NPs. (a) AFM image, (b) thickness profiles and (c) TEM image of BiOI QDs. (d) SEM image and (e) TEM image of MB NPs. (f) TEM image of MVs. (g) TEM image and EDS elemental mapping of O, P, Mn, and Bi of MB@MV NPs. (h) SDS-PAGE analysis of protein retained on the MVs and MB@MV NPs. (i) XPS survey spectra of MB@MV NPs. The high-resolution XPS spectra for (j) Bi 4f, (k) Mn 2p, and (l) P 2p of the MB@MV NPs.

3.2. In vitro assessment of O₂ release, MnO₂ degradation, and •OH generation

The long-term stability of MB@MV NPs was investigated by incubating them in DMEM containing 10 % FBS and subsequently their hydrodynamic diameter through DLS analysis. As shown in Fig. 2a, the particle size of MB@MV NPs in the medium remained relatively stable over time, with no significant agglomeration observed. This result demonstrated that the NPs possess excellent dispersion and stability, which is crucial for their potential *in vivo* applications. In addition, considering that MnO₂ can decompose into water-soluble Mn²⁺ under weakly acidic conditions and produce O₂ by consuming H₂O₂, we investigated the degradation of MB NPs in simulated normal tissue (pH 7.4, 1 μM H₂O₂), TME (pH 6.5, 100 μM H₂O₂), and intracellular tumor (pH 5.5, 1 mM H₂O₂) environments [28,48]. As illustrated in Fig. 2b, complete hollow NP structures were observed after incubation at pH 7.4 with 1 μM H₂O₂, indicating good stability in a normal tissue microenvironment. However, partial degradation of the NPs occurred after incubation at pH 6.5 with 100 μM H₂O₂ for 2 h. The structure of NPs almost completely collapsed in an environment simulating the tumor intracellular level (pH 5.5, 1 mM H₂O₂).

Malignant proliferation of tumors severely exhausts the local supply of O₂, leading to insufficient O₂ levels in the TME. This hypoxic state affects the metabolism and physiology of tumor cells, often disrupting redox homeostasis. Consequently, the levels of H₂O₂ in tumor cells (1

mM) and TME (50–100 μM) are significantly higher than that of normal tissues (<0.7 μM) [48,49]. MnO₂ can generate O₂ and Mn²⁺ by reacting with locally elevated H₂O₂ in tumor cells, alleviating intracellular hypoxia to ensure X-ray induced DNA damages to permanent ones, thereby enhancing the efficiency of tumor cells eradication. Fig. 2c summarized the O₂ release from MB@MV NPs after incubation with PBS, FBS and H₂O₂ over various time periods. There was almost no significant O₂ production after incubation with PBS and FBS for 15 min, and only minimal O₂ production was observed even after the addition of H₂O₂ (1 μM). In contrast, after a 5 min incubation with 1 mM H₂O₂, the dissolved O₂ increased to approximately 11.4 mg/L. The catalase-like activity of MB@MV NPs accelerated H₂O₂-responsive release of O₂, suggesting superior potential for site-specific and on-demand O₂ release to enhance RT sensitization. Furthermore, the intracellular O₂ levels were detected by monitoring fluorescence intensity changes by using RDPP as the trapping agent of O₂. Fig. 2d showed the CLSM observation after MB@MV NPs were incubated with CT26 cells. PBS-treated CT26 cells showed bright red fluorescence, representing the hypoxic state. Obviously, MB@MV NPs treatment displayed inconspicuous red fluorescence under hypoxic and normoxic states, indicating significant O₂ generation resulting in the quenching of the red fluorescence. Fig. S3 summarized the fluorescence semiquantitative analysis, under hypoxic conditions, the red fluorescence intensity of PBS treatment was 3.5 times higher than that of MB@MV NPs incubation, demonstrating the relief of the intracellular hypoxic environment.

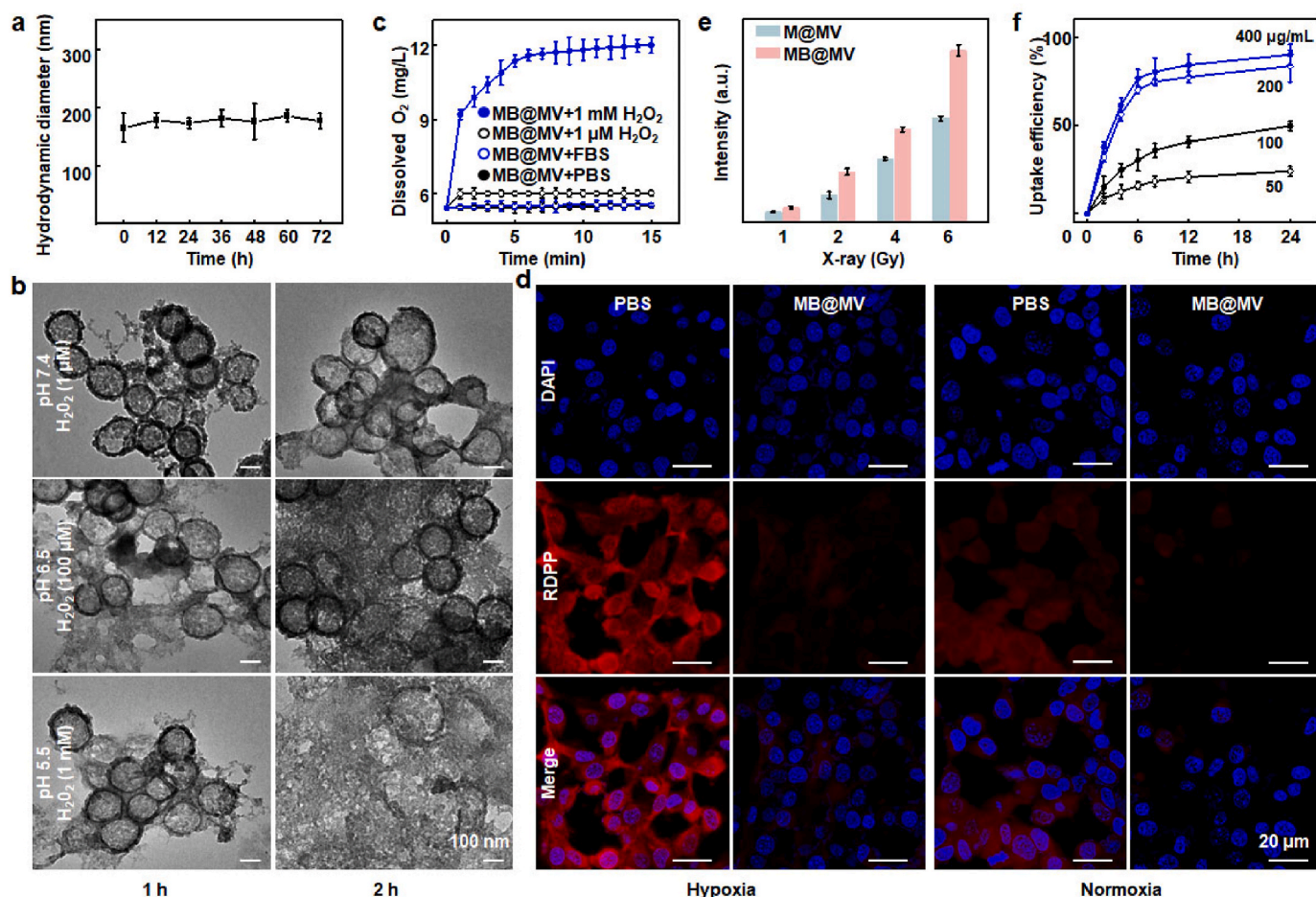


Fig. 2. In vitro O₂ Generation, MnO₂ degradation, •OH generation, and cell uptake efficiency of MB@MV NPs. (a) Change in hydrodynamic diameter of MB@MV NPs after 72 h of incubation in DMEM containing 10 % FBS. (b) TEM images of MB NPs in normal tissues (pH 7.4, 1 μM H₂O₂), TME (pH 6.5, 100 μM H₂O₂), and intracellular tumors (pH 5.5, 1 mM H₂O₂). (c) The O₂ generation under different conditions for MB@MV. (d) CLSM images of RDPP staining in CT26 cells under hypoxia and normoxia conditions. (e) The •OH generation capability of M@MV and MB@MV NPs under various irradiation doses (1, 2, 4, and 6 Gy). (f) Cellular uptake efficiency at various time points following the incubation of MB@MV NPs (50–400 μg/mL) with CT26 cells. (n = 3).

The $\bullet\text{OH}$ generation efficacy of NPs under X-ray irradiation was examined using TA as a capture agent. M@MV NPs without BiOI were prepared to investigate the effect of Bi elements on X-ray absorption. Fig. 2e showed the fluorescence spectra of $\bullet\text{OH}$ after incubation of MB@MV and M@MV NPs in H_2O_2 solution at different doses of X-ray irradiation (1, 2, 4, and 6 Gy). The fluorescence intensity of MB@MV NPs was significantly higher than that of M@MV NPs treatment, which was attributed to the enhanced absorption of X-rays by the BiOI in MB@MV NPs, resulting in higher levels of $\bullet\text{OH}$ and contributing to the killing of cancer cells.

3.3. Cell uptake of MB@MV NPs

To verify the antitumor effect, the internalization ability of MB@MV NPs was examined on CT26 cells. MVs possess a bilayer lipid structure similar to that of the cell membrane, and enhanced intracellular accumulation through macropinocytosis and clathrin-mediated endocytosis [50].

Fig. 2f summarized the uptake efficiencies of Did fluorescently labeled MB@MV/Did NPs (50–400 $\mu\text{g}/\text{mL}$) after incubation with CT26 cells for up to 24 h. CT26 cells exhibited a concentration and time-dependent phagocytosis behavior, showing a high uptake efficiency of about 70.1 % during the first 6 h after incubation with NPs at 200 $\mu\text{g}/\text{mL}$. Cellular uptake levels of MB@MV/Did NPs gradually reached 83.5 % after 24 h of incubation. Even at a concentration of 400 $\mu\text{g}/\text{mL}$ of MB@MV NPs, the uptake efficiency did not show a significant improvement. Accordingly, a concentration of 200 $\mu\text{g}/\text{mL}$ was selected for subsequent cell experiments. Fig. S4 displayed CLSM images of CT26 cells after incubation with 200 $\mu\text{g}/\text{mL}$ of MB@MV/Did NPs and

MB@lip/Did NPs (liposome-coated MB) for 12 h. More intense red fluorescence was observed in the cytoplasm after 6 h of MB@MV/Did NPs treatment compared to MB@lip/Did NPs, which was attributed to interactions with surface receptors promoting targeted delivery to CT26 cells. These results suggested that MVs biomimetic modification facilitates tumor cell uptake of MB@MV NPs and that co-culturing for 6 h is sufficient for optimal cellular uptake.

3.4. In vitro antitumor efficiency of MB@MV NPs

The ROS generation in CT26 cells during X-ray irradiation was investigated by using DCFH-DA as indicator, which was oxidized into 2',7'-dichlorofluorescein molecules with intense green fluorescence [32]. As shown in Fig. 3a, compared with weak green fluorescence in PBS treatment, there was enhanced fluorescence emission after RT and MB@MV NPs treatment, and obvious green fluorescence was detected after M@MV/RT and MB/RT treatment. Notably, the most intense strong green fluorescence was observed in CT26 cells after treatment with MB@MV/RT, probably ascribed to the BiOI-enhanced X-ray absorption and MVs-mediated targeted phagocytosis-elevated ROS generation. The abundant ROS generation inspired us to further explore the antitumor effect of MB@MV/RT treatment. As described in Fig. 3b, MB@MV/RT treatment showed obvious X-ray dose-dependent antitumor performance, and almost all CT26 cells were killed for 6 Gy after MB@MV/RT treatment. Fig. 3c summarized the CT26 cells survival after different treatments. Compared with PBS treatment, there was reduced CT26 cells survival after MB@MV (63.3 %) and RT (52.2 %) treatment, while a significant antitumor effect of M@MV/RT exhibited 29.6 % viable CT26 cells ($p < 0.01$), attributed to intracellular released O_2

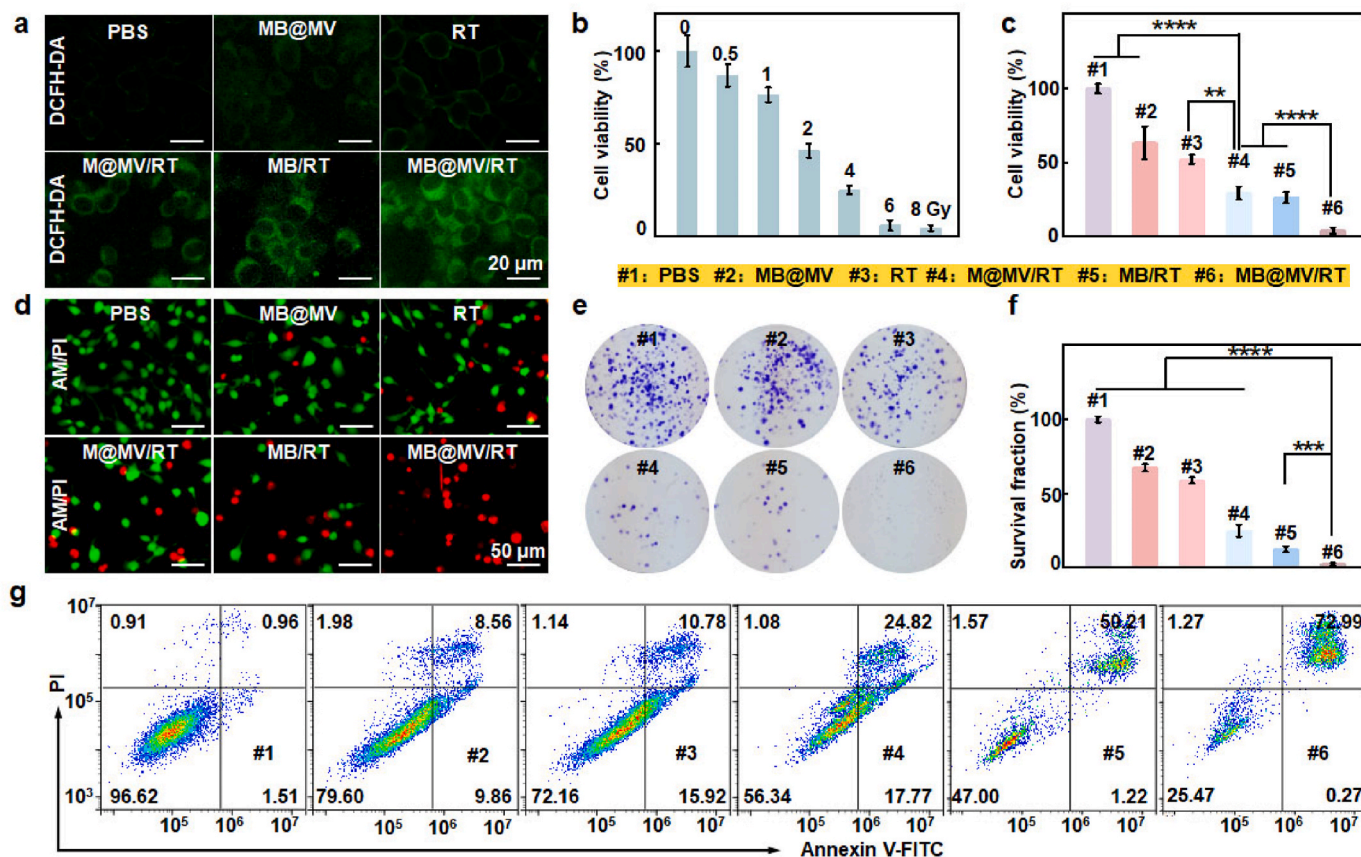


Fig. 3. In vitro antitumor efficiency of MB@MV NPs. (a) CLSM images of DCFH-DA stained CT26 cells after different treatments. (b) Cell viability of CT26 cells exposed to various irradiation doses (0, 0.5, 1, 2, 4, 6, and 8 Gy) in the presence of MB@MV NPs (200 $\mu\text{g}/\text{mL}$). (c) Cell viability, (d) Calcein-AM/PI staining, (e) colony formation assay, (f) corresponding survival fraction, and (g) percentage of apoptosis in CT26 cells after different treatments (NPs: 200 $\mu\text{g}/\text{mL}$, RT: 6 Gy). ($n = 3$, $P^{****} < 0.0001$, $P^{***} < 0.001$, $P^{**} < 0.01$).

stabilizing the DNA damage fixation and enhancing the cytotoxic effect of X-ray on CT26 cells. The cell survival of MB/RT treatment decreased to 26.7 %, due to the BiOI in NPs improving X-ray deposition and achieving radiosensitization.

Importantly, MB@MV/RT treatment showed almost complete tumor cell destruction, attributed to MVs-mediated the enhanced phagocytosis effect (Fig. S4) and O₂/BiOI-assisted antitumor efficacy enhanced the RT outcomes. Moreover, to visualize the antitumor activity, lived/dead (calcein-AM/PI) staining of CT26 cells was performed after different treatments. As shown in Fig. 3d, substantial live CT26 cells were observed with bright green fluorescence after PBS treatment, while MB@MV/RT treatment displayed significantly enhanced red fluorescence compared to other groups. Fig. 3e displayed the cell cloning experiments to demonstrate the radiotherapy sensitization effect. MB@MV/RT had a superior effect on inhibiting tumor cell proliferation than those of MB/RT, M@MV/RT, MB@MV, RT, and PBS treatment. Fig. 3f summarized the colonies of viable CT26 cells after different treatments. Compared with PBS treatment (100 %), enhanced antitumor activity was observed after MB@MV (67.5 %), RT (59.0 %), M@MV/RT (25.0 %), and MB/RT (12.5 %) treatments, while MB@MV/RT exhibited 2.5 % survival CT26 cells ($p < 0.001$). Fig. 3g showed the apoptosis experiment, which demonstrated the apoptosis effects of different treatments. Compared with PBS (2.5 %), MB@MV (18.4 %), RT (26.7 %), M@MV/RT (42.6 %), and MB/RT (51.4 %), the apoptosis rate of MB@MV/RT was 73.3 %, indicating that MB@MV/RT has a good radiosensitization effect. These results indicated that the combined strategy of O₂ supply and doping with high-Z elements greatly improves the effectiveness of radiotherapy and further contributes to the therapeutic efficacy through MVs delivery, showing great potential for *in vivo* applications.

3.5. Antitumor mechanism investigation of MB@MV NPs

The superior CT26 cell killing capacity inspired us to explore its destruction mechanism. X-ray have been confirmed to break the double-strand in DNA, causing the expression of γ -H₂AX in cell nuclei. Fig. 4a showed the immunofluorescence staining of γ -H₂AX (red) with double-staining DAPI (blue). Compared to unobservable red fluorescent regions in CT26 nuclei after treatment with PBS, few red fluorescence signals were detected after MB@MV and RT treatment, indicating relatively weak DNA damage. Enhanced DNA damage was observed in M@MV/RT treatment, attributed to MVs-mediated phagocytosis and O₂-fixed DNA damage. Due to BiOI enhancing X-ray absorption, MB@MV/RT treatment presents significantly increase γ -H₂AX levels compared to CPT (positive control, 5 μ M) treatment and other group, confirming their ability to induce DNA damage. Quantitative fluorescence analysis was next conducted (Fig. 4b), the red fluorescence intensity in the MB@MV/RT group was higher than those of MB@MV, RT, M@MV/RT, and MB/RT treatments, showing a 15.3-fold enhancement compared to that of PBS treatment.

Given that the amplification of intracellular oxidative stress could induce mitochondrial dysfunction [51], the mitochondrial membrane potential was evaluated using JC-1 kit staining. High mitochondrial membrane potential led to JC-1 accumulation in the matrix resulting in enhanced red fluorescence, while low potential resulted in green fluorescence due to a lack of accumulation. As shown in Fig. 4c, MB@MV/RT treatment exhibited stronger green fluorescence compared to PBS, MB/RT, M@MV/RT, RT, MB@MV, and positive control CCCP (10 μ M) treatment, demonstrating that MB@MV NPs effectively reduce mitochondrial membrane potential, consistent with their pro-apoptotic effects. Fluorescence quantitative analysis showed similar

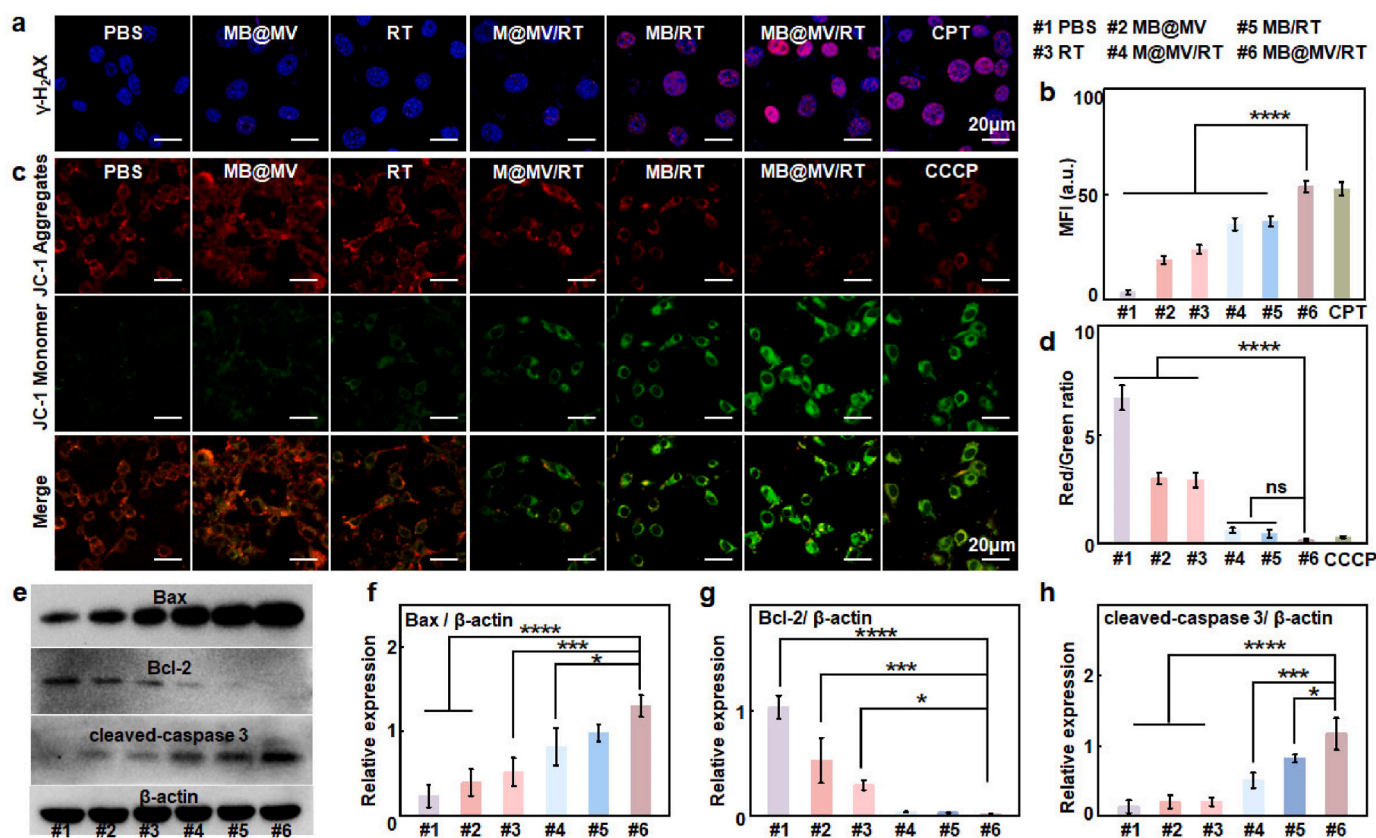


Fig. 4. Antitumor mechanism investigation of MB@MV NPs. (a) Immunofluorescence images and (b) fluorescent quantification analysis of γ -H₂AX in CT26 cells after different treatments (NPs: 200 μ g/mL, CPT: 5 μ M, RT: 6 Gy), (c) CLSM images and (d) fluorescence quantification analysis of JC-1 staining CT26 cells after different treatments (NPs: 200 μ g/mL, CCCP: 10 μ M, RT: 6 Gy), (e) Western blot images of apoptosis-related proteins, and quantitative analysis of (f) Bax/ β -actin, (g) Bcl-2/ β -actin, and (h) cleaved-caspase 3/ β -actin. ($n = 3$, $P^{****} < 0.0001$, $P^{***} < 0.001$, $P^* < 0.05$).

observations. The Red/Green ratio intensity of MB@MV/RT group even lower the CCCP (10 μ M) treatment, and showing 35.3 times lower than that of PBS treatment (Fig. 4d). These results indicated that MB@MV/RT significantly reduced the mitochondrial membrane potential of CT26 cells ($p < 0.0001$). Therefore, the destruction of tumor cells might mainly result from DNA damage and mitochondrial dysfunction through O₂ and BiOI-enhanced radiotherapy sensitization. It should be noted that mitochondrial membrane permeability transition may cause the release of cytochrome C, followed by activating the caspase cascade to induce cell apoptosis [52]. As shown in Fig. 4e, MB@MV/RT treatment led to the overexpression of pro-apoptotic proteins Bax and inhibited the anti-apoptotic protein Bcl-2 levels, with the most noticeable changes in expression occurring compared to other treatments. Consistent results

showed that activation of cleaved-caspase 3, a key executor in apoptosis, was highest in the MB@MV/RT treatment group. The ImageJ-based quantitative analysis of Bax (Fig. 4f), Bcl-2 (Fig. 4g), and cleaved-caspase 3 (Fig. 4h) showed a consistent trend with Western blotting observations. Accordingly, our findings suggested that MB@MV NPs can cause apoptosis in CT26 cells induced by low doses (6 Gy) of X-ray radiation through DNA damage and mitochondrial dysfunction. While previous studies have explored high-Z nanomaterials (e.g., Au, Bi) or hypoxia-modulating agents (e.g., MnO₂) individually [53,54], the MB@MV NPs integrate these functionalities into a single platform, achieving synergistic tumor suppression and immune activation. This innovative approach not only enhances therapeutic efficacy through combined radiosensitization and hypoxia alleviation but also initiates a

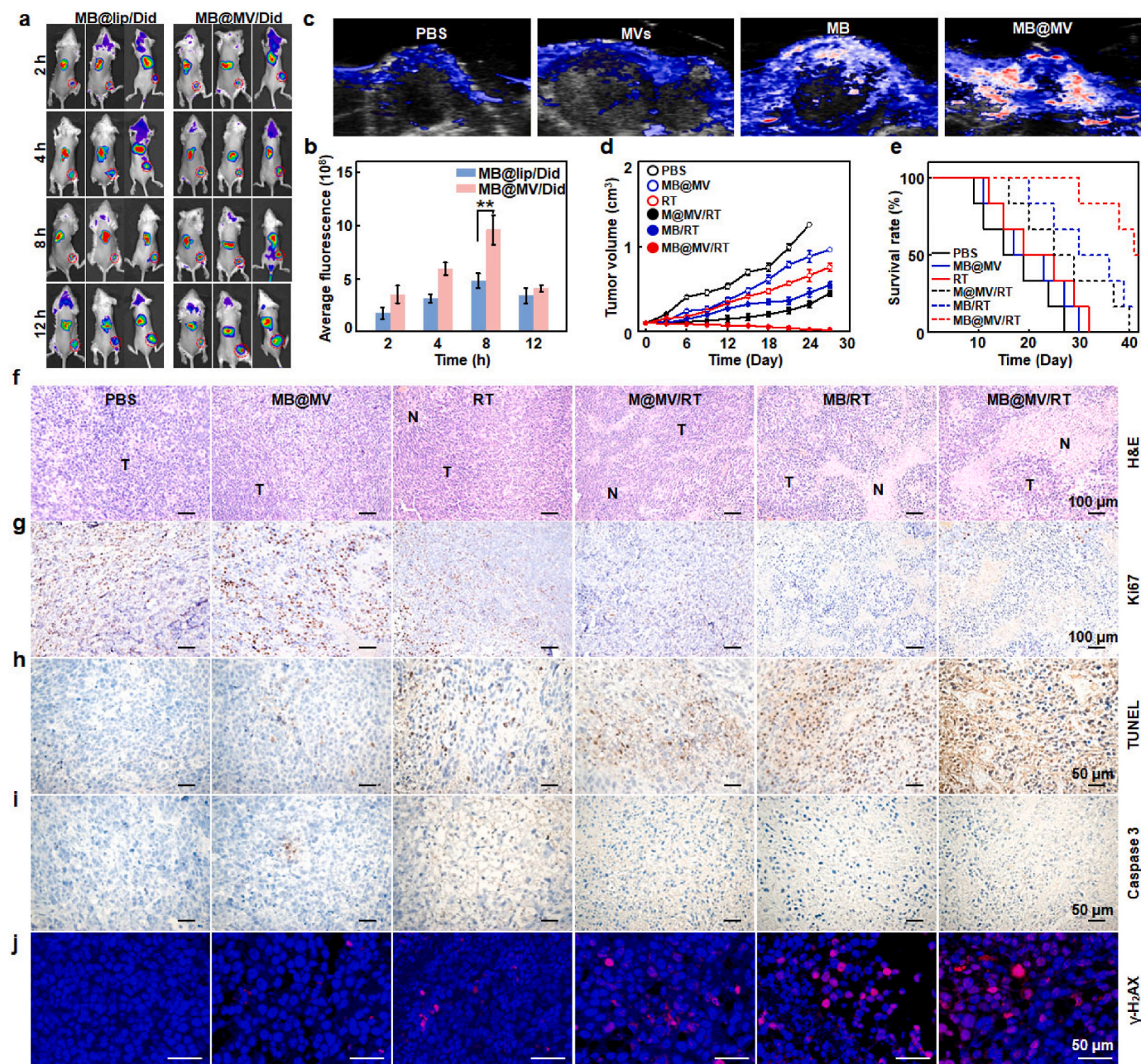


Fig. 5. *In vivo* antitumor effect of MB@MV NPs. (a) *In vivo* fluorescence images of tumor-bearing mice after intravenous injection with Did labeled NPs for various time intervals ($n = 3$). (b) Semi-quantitative fluorescence analysis of MB@lip/Did and MB@MV/Did in tumors at various time points ($n = 3$). (c) Representative tumoral PA images after different treatments. (d) Variations of tumor volume of tumor-bearing mice after different treatments at different time intervals. (e) Survival rate of tumor-bearing mice after different treatments. (f) H&E staining images reveal necrotic areas ("N") and tumor mass ("T") after different treatment. (g) IHC staining images of Ki67, (h) TUNEL, (i) Caspase 3 and (j) immunofluorescence staining images of γ -H₂AX in tumor sections after different treatments. ($n = 6$).

robust anti-tumor immune response, representing a significant advancement in the field of cancer nanomedicine.

3.6. *In vivo* antitumor effect of MB@MV NPs

The superior *in vitro* anti-tumor effect of MB@MV NPs motivates us to continue investigating its potential for *in vivo* application. The tumor targeting of MB@MV NPs was explored in a tumor-bearing mouse model by subcutaneously injecting CT26 cells into Balb/c mice. Fig. 5a exhibited real-time fluorescence images of live mice, which were captured at predetermined points after intravenous administration of Did-labeled MB@MV/Did NPs and MB@lip/Did NPs. The imaging results revealed significantly enhanced tumor accumulation of MB@MV/Did NPs in all experimental mice compared to the MB@lip/Did group. The quantitative analysis of fluorescence intensity demonstrated detectable signals at the tumor site as early as 2 h post-injection of MB@MV/Did NPs, with a time-dependent increase in fluorescence intensity. The intensity reached its peak at 8 h post-injection, at which point the maximum fluorescence intensity in the MB@MV/Did NPs group was approximately 2-fold higher than that in the MB@lip/Did NPs group, indicating superior tumor-targeting efficiency (Fig. 5b). Furthermore, after administration for 8 h, mice were euthanized, and the major tissues (liver, heart, spleen, lungs, kidneys, and tumor) were harvested for imaging. The results indicated that, in addition to tumor tissues, MB@MV/Did NPs were primarily distributed in the liver and kidneys, due to the high entrapping efficiency of the reticuloendothelial system. Compared to the MB@lip/Did NPs group, MB@MV/Did NPs displayed significantly stronger fluorescence signals in the tumor tissues, implying the target effect of MB@MV/Did NPs (Figs. S5a and b). It should be noted that the tumor-targeting ability of MB@MV/Did NPs mediated by MV may be achieved through the enhanced permeability and retention (EPR) effect [55], or by hitching a ride on neutrophils [56].

To investigate whether MB@MV NPs could alleviate tumor hypoxia and convert hemoglobin to oxyhemoglobin (HbO₂), and corresponding blood HbO₂ levels in tumors were monitored using PA imaging. As shown in Fig. 5c, tumor tissues treated with PBS or MVs exhibited a significantly hypoxic state. However, MB NPs injection alleviated hypoxia to some extent. In contrast, the administration of MB@MV NPs resulted in a significant increase in blood HbO₂ levels, notably alleviating hypoxia in tumor tissues. This improvement can be attributed to the tumor-targeting capabilities of MVs.

Encouraged by the effective tumor tissue accumulation and the improvement of the hypoxic TME, the antitumor effect of MB@MV/RT was further investigated in terms of tumor volume, tumor weight, animal survival, histological and IHC staining, using MB/RT, M@MV/RT, RT, MB@MV, and PBS as controls. Fig. 5d summarized tumor growth following various treatments. The tumors treated with PBS increased rapidly in size from 100 to approximately 1260 mm³ over the course of 24 days. Additionally, the MB@MV NPs treatment showed limited effectiveness in inhibiting tumor growth. O₂ enhanced RT apparently impaired tumor expansion to about 320 mm³ after M@MV/RT treatment for 24 days, and the combination of BiOI and O₂ therapy after MB@MV/RT treatment completely inhibited tumor growth. The tumor volume even decreased somewhat after MB@MV/RT treatment during the entire investigation period. As shown in Fig. S6, the change in tumor weight in mice after 24 days of treatment also further indicated the superior anti-tumor ability of MB@MV/RT treatment. Fig. 5e displayed the survival status of mice after different treatments. Compared to PBS treatment, MB@MV NPs treatment showed a median survival time of around 17 days, which was extended to 25 days after M@MV/RT treatment. The median lifespan of tumor-bearing mice after MB@MV/RT treatment reached 41 days, which was much longer than that after MB/RT treatment (30 days).

H&E staining of tumors illustrated the antitumor effects following various treatments over 24 days (Fig. 5f). The MB@OMV/RT treatment

enhanced tumor cell destruction, with increased necrosis, vacuolation, nuclear atrophy, and cell reduction compared to other treatments. Cell proliferation was assessed using IHC staining for Ki-67 (Fig. 5g). The proliferative cell counts following MB@OMV/RT treatment were significantly lower than those for MB/RT (36.2 %), M@OMV/RT (42.1 %), RT (57.2 %), MB@OMV (62 %), and PBS (81.5 %). The area stained positively for TUNEL was significantly larger in the MB@OMV/RT-treated cells compared to the other groups (Fig. 5h). In addition, cell apoptosis was assessed using IHC staining for caspase-3 (Fig. 5i). The MB@MV/RT treatment demonstrated a significantly higher apoptosis rate of 88.4 % compared to MB/RT (71.1 %), M@MV/RT (63.7 %), RT (23.2 %), MB@MV (18.1 %), and PBS (3.4 %) ($p < 0.05$). Immunofluorescence staining for γ -H₂AX revealed a DNA damage rate of 80.7 % in cells treated with MB@MV/RT, which was substantially higher than the rates observed in cells treated with MB/RT (46.9 %), M@MV/RT (44.2 %), RT (28.3 %), MB@MV (15.7 %), and PBS (2.7 %) (Fig. 5j).

3.7. Immune activation of MB@MV NPs

MVs, naturally secreted by bacteria, contain PAMPs similar to those of their parent cells, allowing them to effectively activate the immune system response when introduced into the body [47]. Additionally, studies have shown that treatments like RT, extracorporeal photodynamic therapy, photodynamic therapy, and near-infrared light immunotherapy can also trigger ICD [57]. RT can stimulate tumor cells to release signals that trigger an anti-tumor immune response. To evaluate the capacity of MB@MV/RT to stimulate and activate DCs, we co-cultured PBS, MB@MV, MB/RT, and MB@MV/RT with immature DCs. Flow cytometry results demonstrated significant upregulation of co-stimulatory molecules CD80 and CD86 after MB@MV/RT treatment compared to the other treatments, indicating effective induction of DCs activation and maturation (Fig. S7). Further studies indicated that high-energy rays not only induce tumor cell apoptosis but also prompt CRT to move swiftly from the endoplasmic reticulum to the cell membrane. This exposure allows apoptotic cells to be recognized and engulfed by immune cells, enhancing the body's anti-tumor immune response [58]. To investigate whether MVs and RT induce ICD, we assessed CRT expression using immunofluorescence staining. The MB@MV and MB/RT groups showed increased red fluorescence and CRT expression compared to the PBS group. This suggested that both PAMPs on MVs and RT can elevate the levels of CRT in tumor cells (Fig. 6a). The expression of CRT in the MB@MV/RT group was significantly higher than that in the MB@MV and MB/RT groups ($p < 0.0001$) (Fig. 6b). This finding suggested that the combination of MVs and RT could synergistically enhance CRT expression. Furthermore, ICD triggers tumor cells to release ATP [59], generating a strong anti-tumor immune response, and its release following cell death was mediated by Caspase-3 [60]. After various treatments of CT26 cells, ultrasound was used to lyse the tumor cells, and intracellular ATP levels were measured. Results revealed that the ATP content in the MB@MV/RT group significantly decreased to 0.045 $\mu\text{mol}/10^6$ cells, representing only 30.8 % of the ATP levels in the PBS group, indicating that the most ATP was released after MB@MV/RT treatment, which triggered a stronger anti-tumor immune response (Fig. 6c). Overall, MB@MV/RT demonstrates a superior anti-tumor immune effect.

Encouraged by the activation of DCs by MB@MV/RT *in vitro*, we investigated its effects on the immune system in mice. Tumor tissues and draining lymph nodes were collected from treated tumor-bearing mice. Flow cytometry analysis of single-cell suspensions from tumor-draining lymph nodes revealed that the MB@MV NPs and MB/RT groups upregulated the expression of the co-stimulatory molecules CD80 and CD86. Notably, MB@MV/RT yielded the most pronounced effect on DCs activation (Fig. 6d). Quantitative analysis showed that the PBS group expressed only 4.9 % of CD80 and CD86. However, in the MB@MV NPs group, the expressions increased to 8.2 %, and in the MB/RT group, they further increased to 10.1 %. In contrast, MB@MV/RT induced a 15.5 %

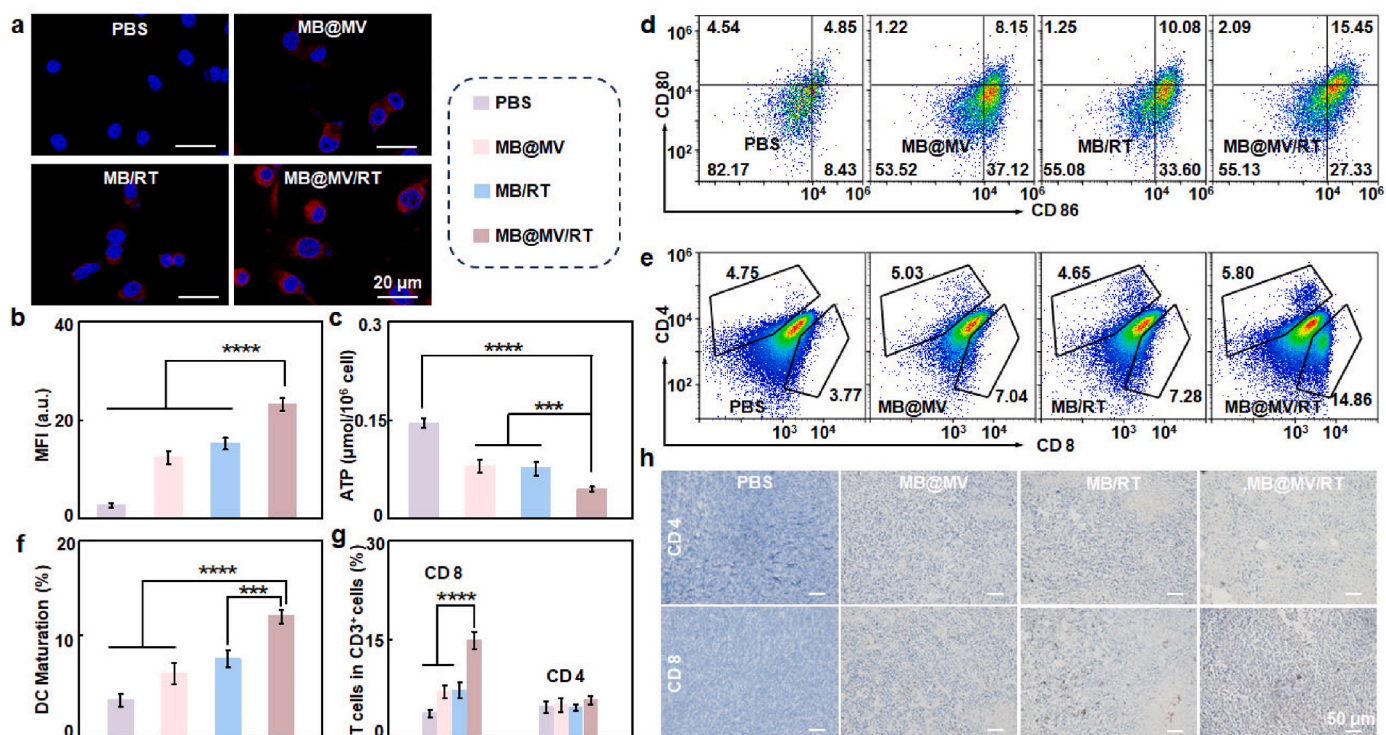


Fig. 6. The immune response by MB@MV NPs. (a) CRT expression and (b) fluorescence quantification of CT26 cells after different treatments. (c) ATP content in CT26 cells after different treatments. (d) Flow cytometry analyze the percentage of CD80⁺/CD86⁺ on the surface of DCs in the mice tumor-draining lymph nodes after various treatments. (e) Flow cytometry analyze the percentage of CD4⁺/CD8⁺ on the surface of T cells in the mouse tumor tissue after different treatments and corresponding quantification for (f) mature DCs and (g) activated T cells. (h) IHC images of CD4⁺ and CD8⁺ T cells from tissues following various treatments. (n = 6, p**** < 0.0001, p*** < 0.001).

increase, demonstrating the synergistic activation of the immune system by MVs and RT (Fig. 6f). Additionally, damage-associated molecular patterns activate antigen-presenting cells like DCs, leading to downstream effects on cytotoxic T lymphocytes (CTLs) and natural killer cells [61]. Similar results were observed in the mouse tumor tissues. Flow cytometry indicated that MB@MV/RT significantly activated CTLs (CD8⁺ T cells) (Fig. 6e). Quantitative analysis showed enhanced expression of CD8⁺ T cells, suggesting effective T cell activation and a boosted immune response (Fig. 6g). Additionally, tumor staining revealed high CD8 expression in the MB@MV/RT treatment group, aligning with the flow cytometry data (Fig. 6h). These findings suggested that MB@MV/RT effectively activates the immune system in mice and works synergistically with radiotherapy to enhance tumor sensitization and inhibition.

3.8. Biosafety profile of MB@MV NPs

Building on previous studies, we assessed the biosafety of MB@MV NPs. We incubated varying concentrations of MB@MV NPs with RBC and found that the hemolysis rates in all groups were below the nano-material safety threshold of 5 % (Fig. 7a). These results demonstrated that MB@MV NPs exhibited good blood compatibility. We further evaluated the biosafety profile of MB@MV NPs after incubation with HUVECs using the CCK-8 cytotoxicity test (Fig. 7b) and calcein-AM/PI staining (Fig. 7c). The CCK-8 assay showed that cell viability remained above 80 % at concentrations below 200 µg/mL, indicating good biosafety. However, at 400 µg/mL, a significant drop in cell viability was observed. This decrease might be attributed to the partial collapse of MB structures, leading to the release of internal BiOI and subsequent reduction in cell viability. In summary, MB@MV NPs demonstrated excellent blood compatibility and biosafety, supporting its potential for safe and stable circulation in the bloodstream. The

weight change of Balb/c mice showed that MB@MV/RT could keep the weight of mice almost stable, alleviating adverse reactions such as emaciation caused by tumors in mice (Fig. S8). To assess the biosafety of MB@MV NPs, we conducted H&E staining on major organ tissues of mice. The results indicated that the treated groups showed no damage to organs and tissues compared to the PBS group (Fig. S9).

A comprehensive hematological and biochemical analysis of blood was assessed after 14 days of MB@MV NPs treatment. As shown in Fig. 7d, the hematological analysis revealed that even at the elevated dose of 400 mg/kg, all measured parameters including white blood cells (WBC, $2.2 \times 10^9/L$), RBC ($8.75 \times 10^{12}/L$), hemoglobin (HGB, 136 g/L), and platelets (PLT, $11.32 \times 10^{11}/L$) remained within normal ranges, indicating no significant adverse effects on blood parameters. Similarly, serum levels of aspartate aminotransferase (AST, 59.8 U/L), alanine aminotransferase (ALT, 137 U/L), creatinine (CREA, 21.4 µM) and UREA (8.75 mM) were within the normal ranges after 14 days of treatment ($p > 0.05$), indicating no liver and kidney toxicity (Fig. 7e). In summary, MB@MV NPs demonstrated significant potential for clinical translation, particularly in enhancing radiotherapy efficacy and tumor-targeted drug delivery through hypoxia alleviation, radiation dose amplification, and anti-tumor immune activation. However, several challenges require resolution, including scalable production, potential immunogenicity, and inconsistent tumor targeting efficiency caused by heterogeneous EPR effects. Future research should prioritize production optimization, immune-related side effect reduction, and combination therapy exploration to maximize therapeutic efficacy. These developments could establish MB@MV NPs as a versatile platform for next-generation cancer treatment.

4. Conclusion

TME-responsible MB@MV NPs were successfully prepared with the

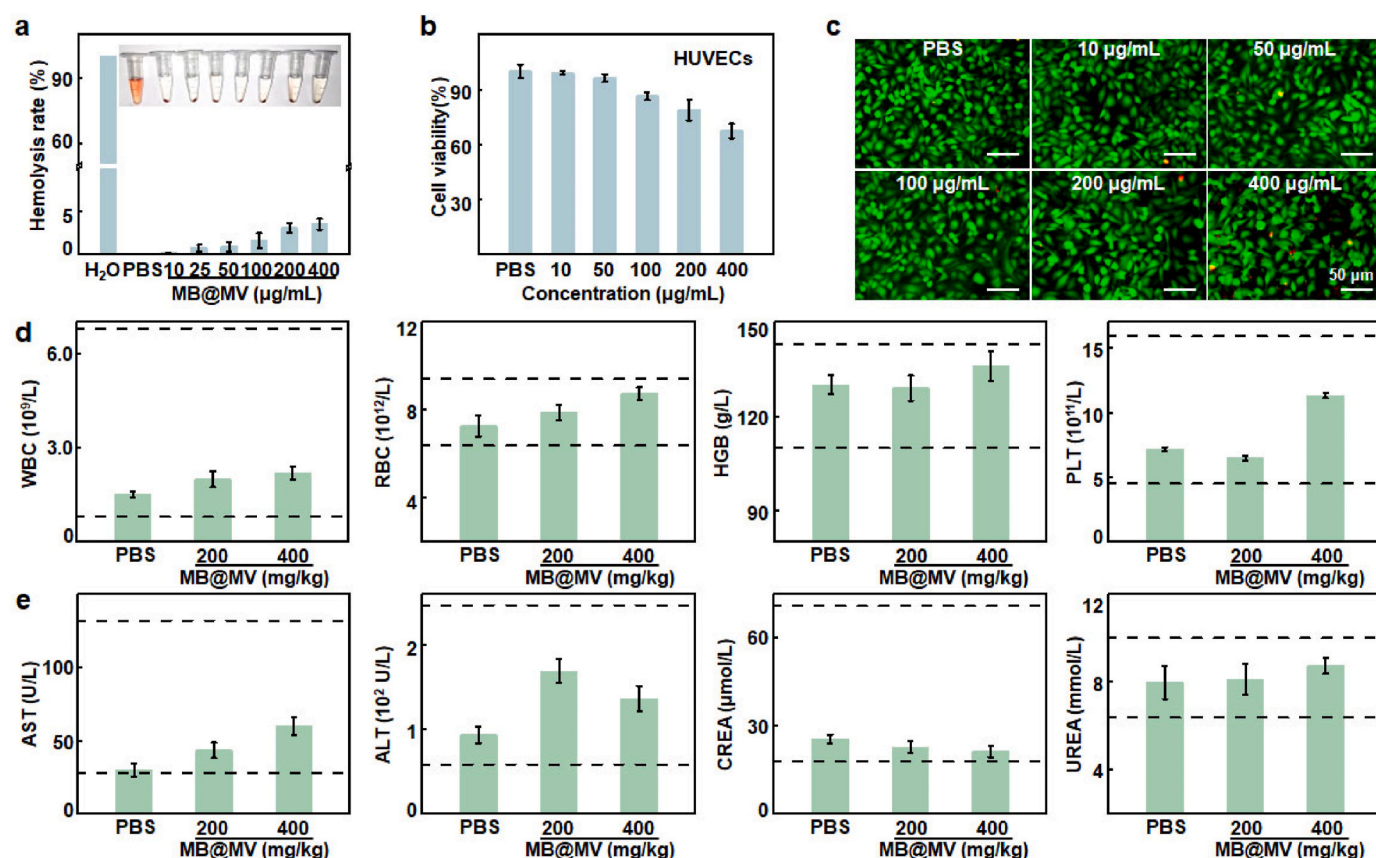


Fig. 7. MB@MV NPs biosafety evaluation. (a) Hemolysis rate of RBC after incubation with MB@MV NPs with different concentrations. (b) Cell viability and (c) calcein-AM/PI staining after incubating HUVECs with MB@MV NPs at different concentrations. (d) Hematological and biochemical analysis of blood from normal mice after MB@MV NPs treatment for 14 days, by using those of PBS treated normal mice as controls (n = 3). The dashed lines indicate normal reference ranges.

aim of targeting tumors and improving the efficacy of radiotherapy. The high-Z element, Bi, allows for greater X-ray deposition in tumor tissues, minimizing toxicity to normal tissues and achieving sensitization. MnO₂ produces O₂ by reacting with H₂O₂ in tumor cells, alleviating hypoxia and thus fixing DNA damage caused by X-rays. MVs further activate the immune response, working synergistically with radiotherapy to enhance anti-tumor effects. *In vitro* and *in vivo* experiments have demonstrated that MB@MV NPs possesses excellent tumor targeting, can effectively eradicate tumors and exhibits good biosafety. The biomimetic NPs developed in this study provide a new approach with potential application in the field of tumor radiotherapy.

CRediT authorship contribution statement

Jiale Chen: Project administration, Methodology, Investigation, Conceptualization. **Pan Ran:** Software, Methodology, Funding acquisition, Formal analysis, Conceptualization. **Yizhao Xu:** Software, Methodology. **Mouna Khouchani:** Writing – review & editing, Project administration, Formal analysis. **Xin Li:** Software, Data curation. **Ling Jian:** Project administration. **Takoui Abdelmajid:** Software, Conceptualization. **Nadia Aittahssaint:** Writing – review & editing. **Qian Yang:** Supervision, Resources. **Jingyi Li:** Visualization, Supervision, Conceptualization. **Long Zhao:** Writing – review & editing, Writing – original draft, Methodology, Investigation, Data curation, Conceptualization.

Declaration of competing interest

The authors declare that they have no known competing financial interests or personal relationships that could have appeared to influence

the work reported in this paper.

Acknowledgements

This work was supported by the Scientific Research Foundation of Science & Technology Department of Sichuan Province (2024NSFSC1972, 2025YFHZ0091), the Health Commission of Sichuan Province Medical Science and Technology Program (24CXTD09), the Chengdu Science and Technology Innovation R&D Project (2024-YF05-02347-SN), the Nuclear Medicine Science and Technology Innovation of China Nuclear Medicine (CYZYB22-18), the Open Fund of Development and Regeneration Key Laboratory of Sichuan Province (24FYYZS05). We also thank the instrument support provided by the nuclear stress medicine center of China National Nuclear Corporation 416 Hospital.

Appendix A. Supplementary data

Supplementary data to this article can be found online at <https://doi.org/10.1016/j.mtbio.2025.101698>.

Data availability

Data will be made available on request.

References

- [1] M.R. Islam, S. Akash, M.M. Rahman, F.T. Nowrin, T. Akter, S. Shohag, A. Rauf, A.S. M. Aljohani, J. Simal-Gandara, Colon cancer and colorectal cancer: prevention and treatment by potential natural products, *Chem. Biol. Interact.* 368 (2022) 110170.

- [2] K.D. Miller, L. Nogueira, T. Devasia, A.B. Mariotto, K.R. Yabroff, A. Jemal, J. Kramer, R.L. Siegel, Cancer treatment and survivorship statistics, *Ca-Cancer J. Clin.* 72 (2022) 409–436.
- [3] W.Y. Zhen, R.R. Weichselbaum, W.B. Lin, Nanoparticle-mediated radiotherapy remodels the tumor microenvironment to enhance antitumor efficacy, *Adv. Mater.* 35 (2023) 2206370.
- [4] G.Z. Yang, W. Li, H.Y. Jiang, X.Y. Liang, Y.G. Zhao, D.H. Yu, L. Zhou, G.J. Wang, H. M. Tian, F.J. Han, L. Cai, J.W. Cui, Low-dose radiation may be a novel approach to enhance the effectiveness of cancer therapeutics, *Int. J. Cancer* 139 (2016) 2157–2168.
- [5] J.N. Xie, L.J. Gong, S. Zhu, Y. Yong, Z.J. Gu, Y. Zhao, Emerging strategies of nanomaterial-mediated tumor radiosensitization, *Adv. Mater.* 31 (2019) e1802244.
- [6] L. Lu, M.Z. Sun, Q.Y. Lu, T. Wu, B.L. Huang, High energy X-ray radiation sensitive scintillating materials for medical imaging, cancer diagnosis and therapy, *Nano Energy* 79 (2021) 105437.
- [7] S.Z. Shi, X. Li, Y. Zhang, H.Y. Huang, J.L. Liu, J. Zhang, Z.G. Wang, H.T. Niu, Y. Zhang, Q.S. Mei, Ultrathin and biodegradable bismuth oxycarbonate nanosheets with massive oxygen vacancies for highly efficient tumor therapy, *Small* 20 (2024) 2307974.
- [8] K.J. Bigos, C.G. Quiles, S. Lunj, D.J. Smith, M. Krause, E.G. Troost, C.M. West, P. Hoskin, A. Choudhury, Tumour response to hypoxia: understanding the hypoxic tumour microenvironment to improve treatment outcome in solid tumours, *Front. Oncol.* 14 (2024) 1331355.
- [9] M. Karabuga, S. Erdogan, K. Filikci, R. Haziroglu, M. Tuncel, M. Cengiz, Evaluation of efficacy of tumor-specific nanoliposomal radiosensitizer in radiotherapy, *J. Drug Deliv. Sci. Technol.* 86 (2023) 104586.
- [10] Y. Pan, L.C. Liu, X.Z. Mou, Y. Cai, Nanomedicine strategies in conquering and utilizing the cancer hypoxia environment, *ACS Nano* 17 (2023) 20875–20924.
- [11] Y.Y. Chen, H. Zhong, J.B. Wang, X.Y. Wan, Y.H. Li, W. Pan, N. Li, B. Tang, Catalase-like metal-organic framework nanoparticles to enhance radiotherapy in hypoxic cancer and prevent cancer recurrence, *Chem. Sci.* 10 (2019) 5773–5778.
- [12] J.J. Liu, Q. Chen, W.W. Zhu, X. Yi, Y. Yang, Z.L. Dong, Z. Liu, Nanoscale-coordination-polymer-shelled manganese dioxide composite nanoparticles: a multistage redox/pH/H₂O₂-responsive cancer theranostic nanoplatform, *Adv. Funct. Mater.* 27 (2017) 1605926.
- [13] F. Pi, X.R. Deng, Q. Xue, L. Zheng, H.X. Liu, F. Yang, T.F. Chen, Alleviating the hypoxic tumor microenvironment with MnO₂-coated CeO₂ nanoplatform for magnetic resonance imaging guided radiotherapy, *J. Nanobiotechnol.* 21 (2023) 90.
- [14] N. Díaz-Garrido, J. Badia, L. Balmó, Microbiota-derived extracellular vesicles in interkingdom communication in the gut, *J. Extracell. Vesicles* 10 (2021) e12161.
- [15] S.A. Badi, S.P. Bruno, A. Moshiri, S. Tarashi, S.D. Siadat, A. Masotti, Small RNAs in outer membrane vesicles and their function in host-microbe interactions, *Front. Microbiol.* 11 (2020) 1209.
- [16] W.D. Nie, A.Q. Jiang, X. Ou, J.X. Zhou, Z.J. Li, C. Liang, L.-L. Huang, G.H. Wu, H.-Y. Xie, Metal-polyphenol “prison” attenuated bacterial outer membrane vesicle for chemodynamics promoted in situ tumor vaccines, *Biomaterials* 304 (2024) 122396.
- [17] X. Wang, J.C. Lee, *Staphylococcus aureus* membrane vesicles: an evolving story, *Trends Microbiol.* 32 (2024) 1096–1105.
- [18] L. Brown, J.M. Wolf, R. Prados-Rosales, A. Casadevall, Through the wall: extracellular vesicles in Gram-positive bacteria, mycobacteria and fungi, *Nat. Rev. Microbiol.* 13 (2015) 620–630.
- [19] A. Chronopoulos, R. Kalluri, Emerging role of bacterial extracellular vesicles in cancer, *Oncogene* 39 (2020) 6951–6960.
- [20] M.Y. Li, Y.T. Wang, H. Liu, X.N. Huang, H.G. Peng, Y. Yang, Z. Hu, J.X. Dou, C. Xiao, J. Chen, W.L. Shang, X.C. Rao, *Staphylococcus aureus* membrane vesicles kill tumor cells through a caspase-1-dependent pyroptosis pathway, *Int. J. Nanomed.* 19 (2024) 4007–4019.
- [21] M. Li, H. Zhou, C. Yang, Y. Wu, X.C. Zhou, H. Liu, Y.C. Wang, Bacterial outer membrane vesicles as a platform for biomedical applications: an update, *J. Controlled Release* 323 (2020) 253–268.
- [22] S. Wu, Y. Huang, J.C. Yan, Y.Z. Li, J.F. Wang, Y.Y. Yang, P.Y. Yuan, X. Ding, Bacterial outer membrane-coated mesoporous silica nanoparticles for targeted delivery of antibiotic rifampicin against gram-negative bacterial infection *in vivo*, *Adv. Funct. Mater.* 31 (2021) 2103442.
- [23] X. Wang, Z. Guo, C.Y. Zhang, S. Zhu, L.L. Li, Z.J. Gu, Y.L. Zhao, Ultrasmall BiOI quantum dots with efficient renal clearance for enhanced radiotherapy of cancer, *Adv. Sci.* 7 (2020) 1902561.
- [24] B. Du, Y.M. Bai, Q.Q. Jiao, M.M. Zhao, M.X. Pang, H.Z. Ma, H.C. Yao, Simultaneous innate immunity activation and immunosuppression improvement by biodegradable nanoplatform for boosting antitumor chemo-immunotherapy, *Chem. Eng. J.* 441 (2022) 136093.
- [25] X.R. Cai, W.X. Liu, J.H. Zhang, Z.R. Li, M.K. Liu, S. Hu, J. Luo, K. Peng, B.F. Ye, Y. Wang, R. Yan, Study of iron complex photosensitizer with hollow double-shell nano structure used to enhance ferroptosis and photodynamic therapy, *Small* 20 (2024) 2470231.
- [26] X.Z. Liu, Z.J. Wen, Y.M. Li, W.R. Sun, X.Q. Hu, J.Z. Zhu, X.Y. Li, P.Y. Wang, J. L. Pedraz, J.-H. Lee, H.-W. Kim, M. Ramalingam, S.Y. Xie, R.R. Wang, Bioengineered bacterial membrane vesicles with multifunctional nanoparticles as a versatile platform for cancer immunotherapy, *ACS Appl. Mater. Interfaces* 15 (2023) 3744–3759.
- [27] R. Wang, Y.J. Yu, M.Y. Gai, A. Mateos-Maroto, S. Morsbach, X. Xia, M.M. He, J. L. Fan, X.J. Peng, K. Landfester, S. Jiang, W. Sun, Liposomal enzyme nanoreactors based on nanoconfinement for efficient antitumor therapy, *Angew. Chem., Int. Ed. Engl.* 62 (2023) e202308761.
- [28] W.W. Zeng, H.J. Zhang, Y.M. Deng, A.T. Jiang, X.Y. Bao, M.Q. Guo, Z.M. Li, M. Y. Wu, X.Y. Ji, X.W. Zeng, L. Mei, Dual-response oxygen-generating MnO₂ nanoparticles with polydopamine modification for combined photothermal-photodynamic therapy, *Chem. Eng. J.* 389 (2020) 124494.
- [29] Y.M. Wang, J.T. He, R. Feng, J.W. Chen, G.G. Xie, S.R. Yu, Y.-X. Wu, K.Q. Tang, Lighting up endogenous H₂O₂ in the tumor microenvironment using a dual-mode nanoprobe for long afterglow and MR bioimaging, *Analyst* 149 (2024) 4230–4238.
- [30] B.H. Chen, P.R. Li, S.S. Zhang, W. Zhang, X.P. Dong, F.N. Xi, J.Y. Liu, The enhanced photocatalytic performance of Z-scheme two-dimensional/two-dimensional heterojunctions from graphitic carbon nitride nanosheets and titania nanosheets, *J. Colloid Interface Sci.* 478 (2016) 263–270.
- [31] P. Ran, W.X. Cao, H. Zheng, S. Xie, G.Y. Zhang, Y. Liu, X.H. Li, Intrabacterial nitroreductase-activated imaging and persistently illuminated photodynamic therapy for intracellular infection theranostics, *Adv. Funct. Mater.* 34 (2024) 2402731.
- [32] O.G. Lyublinskaya, J.S. Ivanova, N.A. Pugovkina, I.V. Kozhukharova, Z. V. Kovaleva, A.N. Shatrova, N.D. Aksenov, V.V. Zenin, Y.A. Kaulin, I.A. Gamaley, N.N. Nikolsky, Redox environment in stem and differentiated cells: a quantitative approach, *Redox Biol.* 12 (2017) 758–769.
- [33] H.Y. Wang, W.B. Wang, L. Liu, M. Wang, G.W. Li, H. Li, B. Li, S.M. Yu, D. Ma, W. Xue, Biodegradable hollow polydopamine@manganese dioxide as an oxygen self-supplied nanoplatform for boosting chemo-photodynamic cancer therapy, *ACS Appl. Mater. Interfaces* 13 (2021) 57009–57022.
- [34] E. t Hart, J. Bianco, M.A.C. Bruin, M. Derieppe, H.C. Besse, K. Berkhout, L.A. Chin Joe Kie, Y. Su, E.W. Hoving, A.D.R. Huitema, M.G. Ries, D.G. van Vuurden, Radiosensitisation by olaparib through focused ultrasound delivery in a diffuse midline glioma model, *J. Controlled Release* 357 (2023) 287–298.
- [35] J.R. Liu, C.X. Li, Z.R. Xie, Q.S. Jia, C.Z. Guo, Z.Y. Wang, S. Wu, F.L. Li, Z.Y. Li, L. G. Hao, Hollow manganese dioxide nanoparticles for drug delivery and imaging, *ACS Appl. Nano Mater.* 7 (2024) 13557–13567.
- [36] X.X. Wang, J.M. Zhou, Y.L. Zhu, C. Yu, D. Sun, Y.F. Yao, L.L. Feng, P.P. Yang, Y. Zhou, Dual-doped metalloporphyrin MOFs-based nanoagent increases low-dose radiotherapy efficacy by apoptosis-ferroptosis for hepatocellular carcinoma, *Chem. Eng. J.* 501 (2024) 157645.
- [37] R. Chai, L.D. Yu, C.H. Dong, Y.P.C. Yin, S. Wang, Y. Chen, Q. Zhang, Oxygen-evolving photosynthetic cyanobacteria for 2D bismuthene radiosensitizer-enhanced cancer radiotherapy, *Bioact. Mater. Lett.* 17 (2022) 276–288.
- [38] J. Liu, J. Zhang, K. Song, J. Du, X. Wang, J.L. Liu, B. Li, R.Z. Ouyang, Y.Q. Miao, Y. Sun, Y.H. Li, Tumor microenvironment modulation platform based on composite biodegradable bismuth-manganese radiosensitizer for inhibiting radioresistant hypoxic tumors, *Small* 17 (2021) e2101015.
- [39] Y. Yang, B. Liu, Y. Liu, J.Q. Chen, Y.J. Sun, X.S. Pan, J. Xu, S.J. Xu, Z. Liu, W. H. Tan, DNA-based MXFs to enhance radiotherapy and stimulate robust antitumor immune responses, *Nano Lett.* 22 (2022) 2826–2834.
- [40] N.H. Huang, X.Y. Tang, W. Meng, Y.H. Lai, X. Zhou, X.Z. Yu, W.H. Zhang, J. X. Chen, Immunogenic radiation therapy for enhanced antitumor immunity via a core-shell nanosensitizer-mediated immunosuppressive tumor microenvironment modulation, *ACS Nano* 17 (2023) 19853–19864.
- [41] J.Q. Qin, T. Yang, J.Y. Li, G.T. Zhan, X. Li, Z.H. Wei, Z.X. Chen, W.X. Zheng, H. B. Chen, X.L. Yang, L. Gan, Bacterial outer membrane vesicle-templated biomimetic nanoparticles for synergistic photothermo-immunotherapy, *Nano Today* 46 (2022) 101591.
- [42] J. Liu, H. Cabral, B. Song, I. Aoki, Z.Y. Chen, N. Nishiyama, Y. Huang, K. Kataoka, P. Mi, Nanoprobe-based magnetic resonance imaging of hypoxia predicts responses to radiotherapy, immunotherapy, and sensitizing treatments in pancreatic tumors, *ACS Nano* 15 (2021) 13526–13538.
- [43] S. Singh, B. Singh, P. Sharma, A. Mittal, S. Kumar, G.S.S. Saini, S.K. Tripathi, G. Singh, A. Kaura, Amino acid functionalized zinc oxide nanostructures for cytotoxicity effect and hemolytic behavior: theoretical and experimental studies, *Mater. Des.* 134 (2017) 10–22.
- [44] W.R. Zhuang, Y.F. Wang, W.D. Nie, Y. Lei, C. Liang, J.Q. He, L.P. Zuo, L.L. Huang, H.Y. Xie, Bacterial outer membrane vesicle based versatile nanosystem boosts the efferoctosis blockade triggered tumor-specific immunity, *Nat. Commun.* 14 (2023) 1675.
- [45] P. Yang, M. Ando, T. Taguchi, N. Murase, Encapsulation of multiple qds into SiO₂ beads by reflux without degrading initial photoluminescence properties, *J. Phys. Chem. C* 114 (2010) 20962–20967.
- [46] Q.Q. Lu, M.M. Hou, X.R. Huang, H.Y. Yu, X.J. Li, J. Jia, Q.Y. Zhou, K. Lv, T.T. Ren, M.C. Liu, Y.T. Zhan, Y.F. Kou, L.K. Dong, T.C. Zhao, X.M. Li, Core@paratroopers nanoassemblies with catalytic cascade for efficient tumor starvation therapy, *Adv. Funct. Mater.* 34 (2024) 2401328.
- [47] Y. Li, R.F. Zhao, K.M. Cheng, K.Y. Zhang, Y.Z. Wang, Y.L. Zhang, Y.J. Li, G.N. Liu, J.C. Xu, J.Q. Xu, G.J. Anderson, J. Shi, L. Ren, X. Zhao, G.J. Nie, Bacterial outer membrane vesicles presenting programmed death 1 for improved cancer immunotherapy via immune activation and checkpoint inhibition, *ACS Nano* 14 (2020) 16698–16711.
- [48] M.X. Wang, F. Zhang, C.Q. Wang, N. Yin, Y.T. Wang, G.X. Qin, Q.L. Xu, J.H. Gong, H.Z. Liu, X.R. Duan, Target-binding accelerated response for sensitive detection of basal H₂O₂ in tumor cells and tissues via a dual-functional fluorescence probe, *Anal. Chem.* 94 (2022) 5962–5969.
- [49] L.W. Wang, X.D. Zhang, Y. Zhen, Z.W. Yang, M.Y. Guo, J.W. Guo, H. Liu, X. Y. Zhang, Z. Wang, A.Z. Wang, Y.W. Lv, J. Zhang, X. Yu, J. Liu, C.Y. Chen, A Molybdenum disulfide nanozyme with charge-enhanced activity for ultrasound-

- mediated cascade-catalytic tumor ferroptosis, *Angew. Chem., Int. Ed.* 62 (2023) e202217448.
- [50] J. Nicolás-Ávila, J.M. Adrover, A. Hidalgo, Neutrophils in homeostasis, immunity, and cancer, *Immunity* 46 (2017) 15–28.
- [51] L. Shu, C. Hu, M. Xu, J.L. Yu, H. He, J. Lin, H.Y. Sha, B. Lu, S. Engelder, M. X. Guan, Z.Y. Song, ATAD3B is a mitophagy receptor mediating clearance of oxidative stress-induced damaged mitochondrial DNA, *EMBO J.* 40 (2021) e106283.
- [52] M. Bonora, C. Giorgi, P. Pinton, Molecular mechanisms and consequences of mitochondrial permeability transition, *Nat. Rev. Mol. Cell Biol.* 23 (2022) 266–285.
- [53] Y.M. Zhang, F. Huang, C.H. Ren, J.J. Liu, L.J. Yang, S.Z. Chen, J.L. Chang, C. H. Yang, W.W. Wang, C.N. Zhang, Q. Liu, X.J. Liang, J.F. Liu, Enhanced radiosensitization by gold nanoparticles with acid-Triggered aggregation in cancer radiotherapy, *Adv. Sci.* 6 (2019) 1801806.
- [54] L.T. Meng, Y.L. Cheng, S.J. Gan, Z.C. Zhang, X.N. Tong, L. Xu, X. Jiang, Y.S. Zhu, J. H. Wu, A. Yuan, Y.Q. Hu, Facile deposition of manganese dioxide to albumin-bound paclitaxel nanoparticles for modulation of hypoxic tumor microenvironment to improve chemoradiation therapy, *Mol. Pharm.* 15 (2018) 447–457.
- [55] O.Y. Kim, H.T. Park, N.T.H. Dinh, S.J. Choi, J. Lee, J.H. Kim, S.W. Lee, Y.S. Gho, Bacterial outer membrane vesicles suppress tumor by interferon- γ -mediated antitumor response, *Nat. Commun.* 8 (2017) 626.
- [56] J. Pan, Z. Wang, X. Huang, J. Xue, S. Zhang, X. Guo, S. Zhou, Bacteria-derived outer-membrane vesicles hitchhike neutrophils to enhance ischemic stroke therapy, *Adv. Mater.* 35 (2023) 2301779.
- [57] S.X. Zhu, Y.M. Wang, J. Tang, M. Cao, Radiotherapy induced immunogenic cell death by remodeling tumor immune microenvironment, *Front. Immunol.* 13 (2022) 1074477.
- [58] A. Scholnik-Cabrera, B. Oldak, M. Juárez, M. Cruz-Rivera, A. Flisser, F. Mendlovic, Calreticulin in phagocytosis and cancer: opposite roles in immune response outcomes, *Apoptosis* 24 (2019) 245–255.
- [59] H.F. Luo, W. Ma, Q. Chen, Z. Yang, Y.L. Dai, Radiotherapy-activated tumor immune microenvironment: realizing radiotherapy-immunity combination therapy strategies, *Nano Today* 53 (2023) 102042.
- [60] Y.W. Ai, Y.T. Meng, B. Yan, Q.Y. Zhou, X.D. Wang, The biochemical pathways of apoptotic, necroptotic, pyroptotic, and ferroptotic cell death, *Mol. Cell.* 84 (2024) 170–179.
- [61] M. Amiri, O. Molavi, S. Sabetkam, S. Jafari, S. Montazersaheb, Stimulators of immunogenic cell death for cancer therapy: focusing on natural compounds, *Cancer Cell Int.* 23 (2023) 200.